

FACULTY
OF MATHEMATICS
AND PHYSICS
Charles University

1

BACHELOR THESIS

2

Martin Vavřík

3

**Simulation and Reconstruction
of Charged Particle Trajectories
in an Atypic Time Projection Chamber**

4

5

Institute of Particle and Nuclear Physics

6

Supervisor of the bachelor thesis: Mgr. Tomáš Sýkora, Ph.D.

7

Study programme: Physics

8

Prague 2025

- ⁹ I declare that I carried out this bachelor thesis independently, and only with the
¹⁰ cited sources, literature and other professional sources. It has not been used to
¹¹ obtain another or the same degree.
- ¹² I understand that my work relates to the rights and obligations under the Act
¹³ No. 121/2000 Sb., the Copyright Act, as amended, in particular the fact that the
¹⁴ Charles University has the right to conclude a license agreement on the use of this
¹⁵ work as a school work pursuant to Section 60 subsection 1 of the Copyright Act.

In date
Author's signature

¹⁶ Dedication.

Title: Simulation and Reconstruction of Charged Particle Trajectories in an Atypical Time Projection Chamber **Added hyphen to avoid overfull hbox**

Author: Martin Vavřík

Institute: Institute of Particle and Nuclear Physics

Supervisor: Mgr. Tomáš Sýkora, Ph.D., Institute of Particle and Nuclear Physics

Abstract: Abstract.

Keywords: key words

¹⁷ Contents

| | | |
|---------------|--|-----------|
| ¹⁸ | Motivation | 3 |
| ¹⁹ | 0.1 ATOMKI Anomaly | 3 |
| ²⁰ | 0.1.1 ATOMKI Measurements | 3 |
| ²¹ | 0.1.2 Other Experiments | 4 |
| ²² | 0.2 X17 Project at IEAP CTU | 6 |
| ²³ | 1 Time Projection Chamber | 9 |
| ²⁴ | 1.1 Charge transport in gases | 9 |
| ²⁵ | 1.1.1 Drift | 9 |
| ²⁶ | 1.1.2 Diffusion | 10 |
| ²⁷ | 1.2 Readout | 11 |
| ²⁸ | 1.2.1 Multi-Wire Proportional Chamber | 11 |
| ²⁹ | 1.2.2 Gas Electron Multiplier | 11 |
| ³⁰ | 1.2.3 Micromegas | 11 |
| ³¹ | 1.2.4 Parallel Plate Chamber | 12 |
| ³² | 1.3 Orthogonal Fields TPC at IEAP CTU | 12 |
| ³³ | 1.3.1 Motivation and Associated Challenges | 12 |
| ³⁴ | 1.3.2 Coordinate Systems and Dimensions | 12 |
| ³⁵ | 1.3.3 Magnetic Field Simulation | 14 |
| ³⁶ | 2 Track Simulation | 17 |
| ³⁷ | 2.1 Microscopic Simulation | 17 |
| ³⁸ | 2.2 Runge-Kutta Simulation | 18 |
| ³⁹ | 3 Track Reconstruction | 19 |
| ⁴⁰ | 3.1 Reconstruction Assuming Steady Drift | 19 |
| ⁴¹ | 3.2 Ionization Electron Map | 21 |
| ⁴² | 3.2.1 Gradient Descent Search | 24 |
| ⁴³ | 3.2.2 Interpolation on the Inverse Grid | 25 |
| ⁴⁴ | 3.3 Discrete Reconstruction | 26 |
| ⁴⁵ | 4 Energy Reconstruction | 28 |
| ⁴⁶ | 4.1 Cubic Spline Fit | 28 |
| ⁴⁷ | 4.2 Circle and Lines Fit | 30 |
| ⁴⁸ | 4.2.1 Two-dimensional fit | 30 |
| ⁴⁹ | 4.2.2 Three-dimensional fit | 32 |
| ⁵⁰ | 4.3 Runge-Kutta Fit | 32 |
| ⁵¹ | Conclusion | 34 |
| ⁵² | Bibliography | 36 |
| ⁵³ | List of Figures | 39 |
| ⁵⁴ | List of Tables | 41 |

56 Motivation

57 A Time Projection Chamber (TPC) is a type of gaseous detector that detects
58 charged particle trajectories by measuring the positions and drift time of ions
59 created in the gas; details are provided in Section 1. The energy of these particles
60 can be inferred from the curvature of their trajectory in the magnetic field.

61 The goal of this thesis is to develop an algorithm for the reconstruction of
62 charged particle trajectories and energy in an atypic TPC with orthogonal elec-
63 tric and magnetic fields, hereafter referred to as the Orthogonal Fields TPC
64 (OFTPC), used in the X17 project at the Institute of Experimental and Applied
65 Physics, Czech Technical University in Prague (IEAP CTU). Furthermore, we
66 present the results of testing this algorithm with different samples of simulated
67 data. (We use the Garfield++ toolkit [1] for simulations in combination with
68 the ROOT framework [2] for data analysis and visualization. Some of our more
69 demanding simulations are run on the MetaCentrum grid [3].)

70 The X17 project in IEAP CTU aims to reproduce measurements of anomalous
71 behavior in the angular correlation distribution of pairs produced by the Internal
72 Pair Creation (IPC) mechanism [4] during the decay of certain excited nuclei
73 (^{8}Be , ^{12}C , and ^{4}He) observed by a team at ATOMKI in Hungary. I would leave
74 this here as a short summary before I explain it in more detail in the sections
75 below.

76 Add citations: X17 project, VdG. Maybe also TPC, etc.

77 0.1 ATOMKI Anomaly

78 Many theories propose the existence of new light bosons that are weakly coupled
79 to ordinary matter [5]. These particles are potential dark matter candidates and
80 could solve other issues with the Standard Model, such as the strong CP problem
81 and the anomalous muon magnetic moment.

82 A possible way of detecting such bosons with a short lifetime is to observe
83 nuclear transitions of excited nuclei. If a boson was emitted during the transition
84 and subsequently decayed into an electron-positron pair, we could observe this
85 as a peak on top of the e^+e^- angular correlation from IPC and External Pair
86 Creation (EPC).

87 0.1.1 ATOMKI Measurements

88 Previously, there were several measurements of IPC in nuclear transitions in ^{8}Be
89 at Institute für Kernphysik (Frankfurt) [6, 7, 8] and at ATOMKI [9, 10] resulting
90 in different anomalies with invariant mass in the range 5–15 MeV. This prompted
91 a development of a better spectrometer.

92 In 2015, a group at ATOMKI led by Attila Krasznahorkay observed an anom-
93 lous IPC in ^{8}Be [11]. They used the $^{7}\text{Li}(p, \gamma)^{8}\text{Be}$ reaction at the $E_p = 1030$ keV
94 proton capture resonance to prepare the 18.15 MeV excited state ($J^\pi = 1^+, T =$
95 $= 0$). This state decays predominantly through M1 transitions to the ground
96 state ($J^\pi = 0^+, T = 0$) and to the 3.03 MeV state ($J^\pi = 2^+, T = 0$) [12].

97 The angular correlation of the e^+e^- pairs created internally in these transitions
98 were measured and compared to the simulation; results from a narrow $E_{\text{sum}} =$
99 = 18 MeV region are shown in Figure 0.1a. The simulation includes boson decay
100 pairs for different boson masses. The disparity parameter y is defined as

$$y = \frac{E_{e^-} - E_{e^+}}{E_{e^-} + E_{e^+}}, \quad (0.1)$$

101 where E_{e^-} and E_{e^+} are the kinetic energies of the electron and positron.

102 Their experimental setup was later upgraded ([details?](#)) and used for new mea-
103 surements. In 2022 the ${}^8\text{Be}$ anomaly was also measured using the $E_p = 441$ keV
104 resonance to produce the 17.64 MeV excited state ($J^\pi = 1^+$, $T = 1$) which again
105 decays primarily to the ground state and the 3.03 MeV state [12]. The anomaly
106 was also measured for $E_p = 650$ and 800 keV where E1 transitions from the direct
107 proton capture dominate [13]. The results for e^+e^- with $E_{\text{sum}} \in [13.5, 20]$ MeV
108 are shown in Figure 0.1b.

109 The newer setup was also used in 2021 to study the ${}^3\text{H}(p, e^+e^-){}^4\text{He}$ reaction at
110 $E_p = 510, 610$ and 900 keV [14], inducing direct and resonant capture populating
111 the overlapping first 20.21 MeV ($J^\pi = 0^+$) and second 21.01 MeV ($J^\pi = 0^-$)
112 excited states [15]. The comparison of simulated and measured e^+e^- pair angular
113 correlations in the $E_{\text{sum}} \in [18, 22]$ MeV region is shown in Figure 0.1c.

114 In 2022, another anomaly was measured in the ${}^{11}\text{B}(p, e^+e^-){}^{12}\text{C}$ process [16].
115 The $E_p = 1388$ keV resonance was used to populate the 17.23 MeV excited state
116 ($J^\pi = 1^-, T = 1$) with a large width $\Gamma = 1.15$ MeV [17]. This state decays
117 mainly through E1 transitions to the ground state $J^\pi = 0^+$ and to the 4.44 MeV
118 state $J^\pi = 2^+$. To compensate for energy losses in the target, five energies in
119 the range $E_p = 1.5\text{--}2.5$ MeV were used. The experimental angular correlation for
120 the 17.23 MeV transition to the ground state is shown in Figure 0.1d.

121 Possible explanations of the anomaly include experimental effects, higher or-
122 der processes in the Standard Model [18, 19] or even a protophobic fifth force
123 mediated by a new 17 MeV boson X17 [20]. [Zhang and Miller: <https://www.sciencedirect.com/science/article/pii/S0370269321000010>](https://www.sciencedirect.com/science/article/pii/S0370269321000010)

125 0.1.2 Other Experiments

126 Since the ATOMKI measurements, several experiments have been initiated to
127 attempt to replicate the results and search for the hypothetical X17 particle.
128 [Here are a few with results. Could cite the ATOMKI review paper here.](#)

129 Two-arm e^+e^- spectrometer in Hanoi

130 The anomaly in ${}^8\text{Be}$ has been observed with $> 4\sigma$ confidence by a team at the
131 Hanoi University of Sciences for $E_p = 1225$ keV [21]. They built a two-arm
132 spectrometer in collaboration with ATOMKI and calibrated it using the 17.6 MeV
133 M1 transition. The results are shown in Figure 0.2.

134 Collisions at Nuclotron in Dubna

135 At the Joint Institute for Nuclear Research in Dubna, signal in the form of en-
136 hanced structures in the $\gamma\gamma$ spectra at ~ 17 and ~ 38 MeV invariant masses

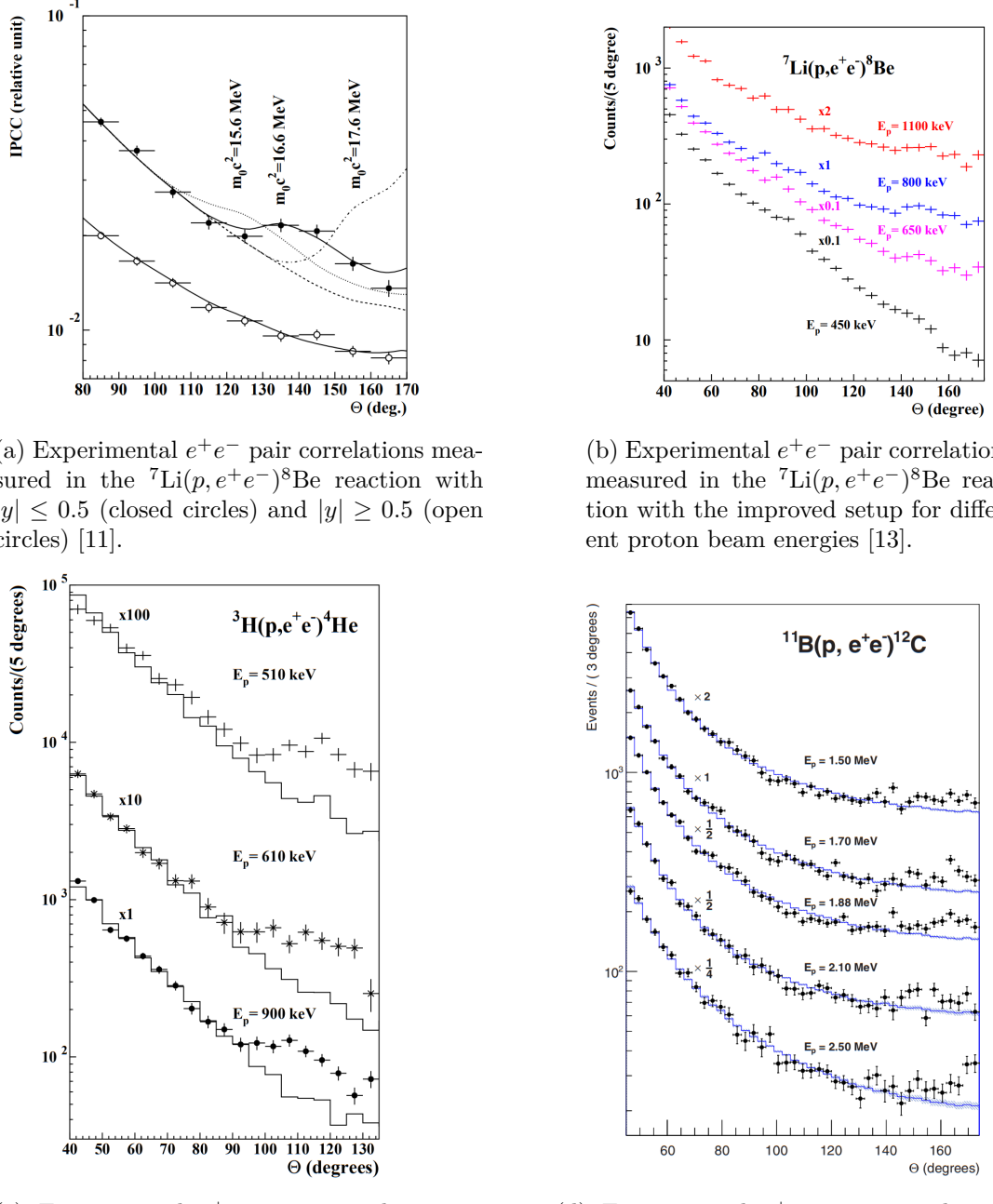


Figure 0.1: The ATOMKI anomalous IPC measured for different nuclei.



Figure 0.2: Results from the Hanoi spectrometer – angular e^+e^- pair correlations measured in the ${}^7\text{Li}(p, e^+e^-){}^8\text{Be}$ reaction at $E_p = 1225$ keV [21].

137 for $p + \text{C}$, $d + \text{C}$ and $d + \text{Cu}$ reactions at momenta 5.5, 2.75, and 3.83 GeV per
 138 nucleon [22]. Monte Carlo simulations support the conclusion that the signals
 139 are a consequence of a decay of unknown particles X17 and E38.

140 The MEG II (Muon Electron Gamma) experiment

141 Experiments using the ${}^7\text{Li}(p, e^+e^-){}^8\text{Be}$ reaction were carried out at the Paul
 142 Scherrer Institute with the MEG II superconducting solenoid spectrometer [23].
 143 Analysis of the data with $E_p = 1080$ keV exciting both of the resonances (beam
 144 fully stopping in the target) found no significant evidence supporting the X17
 145 hypothesis, results are shown in Figure 0.3. An upper bound (at 90% confidence)
 146 on the X17-to- γ branching ratio was set at $1.2 \cdot 10^{-5}$ for the 18.15 MeV state
 147 (larger than the ratio $5.8 \cdot 10^{-6}$ obtained by ATOMKI in 2016). Could add their
 148 90% C.L bounds figure also.

149 0.2 X17 Project at IEAP CTU

150 The aim of the X17 project at the Van der Graaff facility of the Institute of
 151 Experimental and Applied Physics, Czech Technical University in Prague is to
 152 repeat the original ATOMKI experiments with ${}^7\text{Li}$ and ${}^3\text{H}$ targets using an inde-
 153 pendent e^+e^- spectrometer. In order to effectively measure the anomaly, we need
 154 to reconstruct both the energy and the angular correlation of the e^+e^- pairs. The
 155 spectrometer will use three layers of detectors to achieve this – Timepix 3 (Tpx3)
 156 silicon pixel detector and Multi-Wire Proportional Chamber (MWPC) layers for
 157 the angle reconstruction and a Time Projection Chamber (TPC) layer for the en-
 158 ergy reconstruction. The schematics of the prepared detector is in Figure 0.4
 159 Spectrometer CAD drawing (coordinates here or next chapter?). Cite some VdG
 160 paper, mention grant? Using https://cernbox.cern.ch/pdf-viewer/public/rf0oU1nqVLN3acZ/LuzH_submitted.pdf.

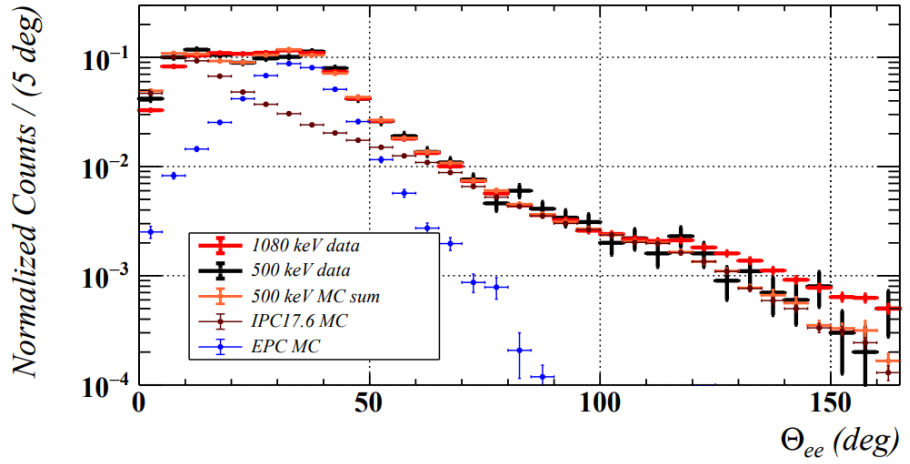


Figure 0.3: Results from the MEG II experiments – angular correlation of e^+e^- pairs with $E_{\text{sum}} \in [16, 20]$ MeV measured in the ${}^7\text{Li}(p, e^+e^-){}^8\text{Be}$ reaction with proton beam energies 500 and 1080 keV. The 500 keV dataset is fitted with Monte Carlo of both the IPC deexcitation and the EPC produced by gammas [23].

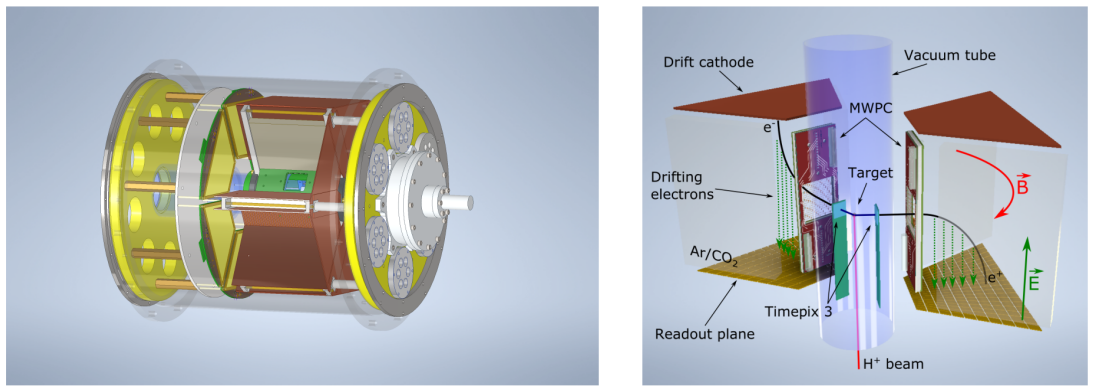


Figure 0.4: Schematics of the detector at the Van der Graaff facility at IEAP CTU.

162 The energy of e^+e^- pair produced in the reaction is given by the energy
163 available E_r in the reaction and can be distributed between them arbitrarily.
164 Nonetheless in the decay of the hypothetical X17 particle, electron and positron
165 should have similar energy and we can therefore use a disparity cut $|y| \leq 0.5$
166 for the disparity parameter (defined in Equation 0.1). Interesting events should
167 rarely have a particle with an energy below $E_r/4$ (roughly 4 MeV). Electrons with
168 such low energies are scattered significantly by even a thin layer of relatively light
169 material, for this reason the Tpx3 layer will be inside of the vacuum tube and the
170 tube will have a thinned aluminum segment or KaptonTM windows.

171 Tpx3 can measure (in each $55 \times 55 \mu\text{m}$ pixel of its 256×256 grid) time-of-arrival
172 (ToA) with 1.6 ns precision and time-over-threshold (ToT) which reflects the de-
173 posited energy. This potentially allows 3D tracking if we increase the chip thick-
174 ness at the cost of increased scattering. The layer can reconstruct the reaction
175 vertex and the angular correlation with high precision.

176 The layer of MWPCs with sensitive area $40 \times 38 \text{ mm}^2$ will be outside of
177 the beam pipe. It will provide an extra point on the particle trajectory which can
178 help with the estimation of the reaction vertex and improve the TPC performance
179 by providing its entry point.

180 The TPCs, which are a subject of this theses, are in a magnetic field of per-
181 manent magnets positioned between them and provide 3D track reconstruction
182 and subsequent momentum and particle identification (its charge, or even type
183 based on its stopping power). They avoid radiative losses thanks to the small
184 interaction with the incident particle. For the readout, triple Gas Electron Mul-
185 tiplier (GEM) will be used. The magnetic field layout in our TPCs is atypical –
186 orthogonal to the electric field inside the chamber, this is why we call them Or-
187 thogonal Fields TPC (OFTPC). Further details about our OFTPCs are provided
188 in section 1.3.

1. Time Projection Chamber

189 Using (2010 – a little old) <https://cds.cern.ch/record/1302071/files/CERN-PH-EP-2010-047.pdf>

190 A Time Projection Chamber (TPC) is a type of gaseous detector that uses
191 the drift in an electric field of free charges (electrons and cations) produced by
192 an ionizing particle to reconstruct its 3D trajectory. When placed inside a mag-
193 netic field, the momentum of the incident particle can be inferred from the curva-
194 ture of its trajectory. Particle identification is also possible using the ionization
195 energy loss inside the TPC.

196 The original TPC used in the PEP-4 experiment at SLAC was a 2×2 m
197 cylinder with a central cathode that produced a strong electric field, making
198 the ionization electrons drift towards one of the bases. The readout consisted
199 of MWPCs, where electrons are accelerated towards the anode wires enough to
200 further ionize the gas and cause an avalanche. Figure?

201 When a charged particle crosses the volume of a TPC, it loses energy by
202 excitation and ionization of the detector gas. Most ionizing collision produce
203 a single ionization electron, sometimes a few secondary electrons are produced
204 close to the collision vertex. In rare cases, the ionization electron has energy
205 large enough to create a measurable track, such an electron is called a δ -electron.
206 Penning transfer (collisions, light – factor 10 for gas gain in Ar/CO₂ viz PDG
207 CERN)?

208 CERES/NA45 – very inhomogeneous magnetic field

211 1.1 Charge transport in gases

212 1.1.1 Drift

213 The produced ionization electrons are accelerated towards the readout by the elec-
214 tric field inside the chamber. At the same time, they lose speed by colliding with
215 the gas particles, quickly reaching a constant (for a given field \mathbf{E}, \mathbf{B}) mean drift
216 velocity. The electrons might be absorbed by electronegative impurities, such as
217 halides and oxygen.

218 In many gases (called "hot", e.g., Ar or CH₄), the drift velocity is much greater
219 than that of their thermal motion thanks to a high proportion of elastic collisions.
220 On the other hand, "cold" gases like CO₂ have a higher proportion of inelastic
221 collisions (e.g., thanks to the excitation of rotational and vibrational states) and
222 therefore much lower drift velocity.

223 The cations produced by the ionization lose a significant portion of their
224 energy during each collision thanks to their large mass. This makes their drift
225 velocity much smaller and their energy is close to thermal. Since their momentum
226 isn't randomized to such extent during collisions, their diffusion is smaller.

227 The drift is also influenced by the magnetic field, Langevin derived a good
228 approximation for the drift velocity vector:

$$\mathbf{v}_d = \left(\frac{\mathbf{E}}{\|\mathbf{E}\|} + \omega\tau \frac{\mathbf{E} \times \mathbf{B}}{\|\mathbf{E}\| \|\mathbf{B}\|} + \omega^2\tau^2 \frac{\mathbf{E} \cdot \mathbf{B}}{\|\mathbf{E}\| \|\mathbf{B}\|} \cdot \frac{\mathbf{B}}{\|\mathbf{B}\|} \right) \frac{q\tau}{m(1 + \omega^2\tau^2)} \|\mathbf{E}\|, \quad (1.1)$$

229 where q is the charge of the particle, m is its mass, τ is the mean time between
 230 collisions and $\omega = \frac{q}{m}\|\mathbf{B}\|$ is the Larmor frequency. In a standard TPC, \mathbf{E} is
 231 nearly parallel to \mathbf{B} and only small corrections are needed. The ion drift is only
 232 negligibly influenced by the magnetic field ($\omega\tau \sim 10^{-4}$ is small). **Lorentz angle**
 233 **for orthogonal fields** $\tan \psi = -\omega\tau$ (deviation from electric field) – maybe mention
 234 in the OFTPC section. Without magnetic field, we can write

$$\mathbf{v}_d = \frac{q\tau}{m}\mathbf{E} = \mu\mathbf{E}, \quad (1.2)$$

235 where μ is called charge mobility.

236 1.1.2 Diffusion

237 Due to random collisions a point-like cloud of electrons or ions will show a Gaussian
 238 density distribution at time t due to the drift in electric field $\mathbf{E} = (0, 0, E_z)$:

$$\rho(x, y, z, t) = (4\pi Dt)^{-\frac{3}{2}} \exp\left(-\frac{x^2 + y^2 + (z - v_d t)^2}{4Dt}\right), \quad (1.3)$$

239 where D is the diffusion coefficient given by

$$D = \frac{\lambda^2}{3\tau} = \frac{\lambda v_d}{3} = \frac{v_d^2 \tau}{3} = \frac{2\varepsilon\tau}{3m}, \quad (1.4)$$

240 where λ is the mean free path and ε the mean energy. The lateral diffusion width
 241 σ_x after a drift distance L can be expressed as

$$\sigma_x^2 = 2Dt = \frac{4\varepsilon L}{3qE}. \quad (1.5)$$

242 The minimal diffusion width is given by lowest possible (thermal) energy of
 243 the particles $\varepsilon_{\text{th}} = \frac{3}{2}kT$:

$$\sigma_{x, \text{min}}^2 = \frac{2kTL}{qE}. \quad (1.6)$$

244 For electrons in "cold gases" (e.g., Ar/CO₂ mixture), the diffusion approaches
 245 this limit up to a certain field intensity (~ 100 V/cm at 1 atm pressure). **For us**
 246 **0.45 mm, quite close to the actual diffusion 0.5-0.7 mm.** In reality, the transversal
 247 diffusion of electrons can be significantly different from their longitudinal diffu-
 248 sion, simulations are necessary to achieve a precise calculation.

249 In most TPCs, the transversal (but not the longitudinal) diffusion is reduced
 250 by the magnetic field (parallel to electric):

$$\frac{D_T(B)}{D_T(0)} = \frac{1}{C + \omega^2 \tau_2^2}, \quad (1.7)$$

251 where C and τ_2 are parameters dependent on the gas. At low B , we can use
 252 an approximation $C \approx 1$ and $\tau_2 \approx \tau$.

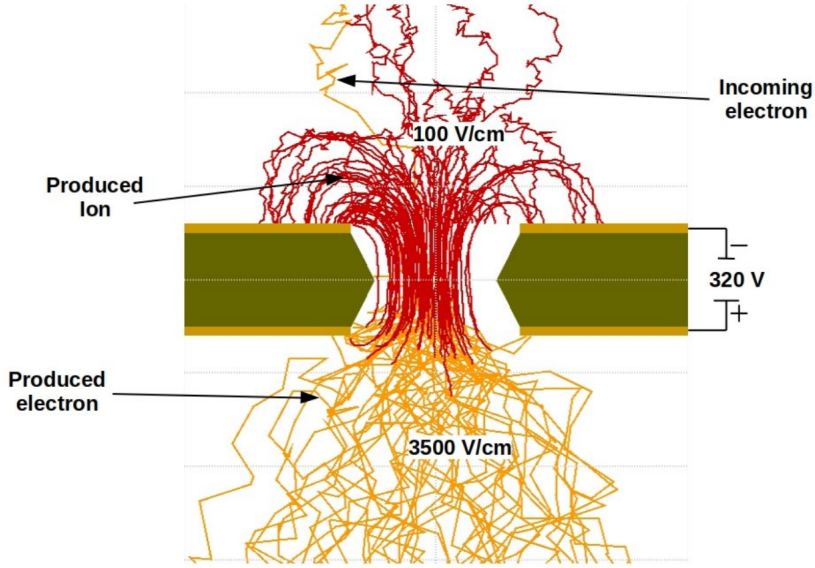


Figure 1.1: Garfield simulation of an avalanche in a GEM hole [24].

253 1.2 Readout

254 1.2.1 Multi-Wire Proportional Chamber

255 In most (2010 – almost all) TPCs operated in experiments Multi-Wire Proportional Chamber (MWPC) was used for the readout. The electrons enter the chamber through a cathode grid and get accelerated in the strong electric field towards 256 the thin anode wires and create a Townsend avalanche, multiplying the signal. 257
 258 **Alternating with field wires?** The trajectory can be reconstructed using pulses 259 from each separate wire. Segmented cathode is also often used for the readout of 260 produced cations. **Gating grid (reduction of space charge effect, blocking backflow 261 of ions?, closed for electrons $B=0$, ΔV , static mode (loss of 25% el.) x opening on 262 trigger)?** (gas amplification > 10000 required for good SNR, 100-200 ns shaping 263 time), figure?

265 1.2.2 Gas Electron Multiplier

266 The Gas Electron Multiplier (GEM) is a thin metal-coated polymer sheet with 267 a high density of small holes. The amplification is achieved by applying voltage 268 on the metal layers, creating a strong electric field inside the holes and causing 269 avalanches. Double or triple stack of GEMs is usually used to create a sufficient 270 gain. From the last foil, the electrons drift to a segmented anode where the signal 271 is read. The backflow of cations is reduced compared to MWPC. An example 272 simulation of an avalanche inside GEM is shown in Figure 1.1. **Parameters?**

273 1.2.3 Micromegas

274 In a MICRO-MEsh GAseous Structure (Micromegas) electrons pass through a fine 275 mesh (made out of very thin wires) into the narrow amplification gap where they 276 are multiplied in the high field and read as signal on the segmented anode. Very

277 high field ($30\text{-}80 \text{ kV/cm}^2$) is necessary to achieve sufficient gain. Cation backflow
278 is heavily suppressed by the mesh.

279 1.2.4 Parallel Plate Chamber

280 ... micowell?

281 1.3 Orthogonal Fields TPC at IEAP CTU

282 At IEAP CTU, we are going to use six identical atypical TPCs with inhomoge-
283 neous toroidal magnetic field orthogonal to the electric field, hereafter referred to
284 as Orthogonal Fields TPC (OFTPC). It has the shape of isosceles trapezoidal
285 prism 16 centimeters high with triple-GEM readout on one of its bases. Dimen-
286 sions of the OFTPC are discussed in detail in section 1.3.2 below. Throughout this
287 thesis, we assume a uniform electric field along the z axis with $E_z = -400 \text{ V/cm}$.
288 Gas mixture used in the detector (70/30) and its effect – some graph with the
289 mixture.

290 1.3.1 Motivation and Associated Challenges

291 The reasons for the unusual field layout are mostly cost related:

- 292 • we use permanent magnets instead of a solenoid and parallel fields are
293 difficult to accomplish this way,
- 294 • granularity of the TPC readout is limited in order to fit one SAMPA/SRS
295 hybrid in each sector – parallel fields would bend the trajectories parallel
296 to the readout requiring more pads and different architecture.

297 In this thesis, we will show that such a setup can reach a similar energy resolution
298 as common cylindrical TPCs while reducing cost.

299 The layout introduces two complications to the track reconstruction – the
300 trajectory in inhomogeneous field is not circular and the drift is distorted by
301 the magnetic field (see Equation 1.1, in our case $\omega\tau \approx 0.08$ for 0.3 T assuming
302 $\mu \approx 0.25 \text{ T}^{-1}$, varies inside the detector). The diffusion in such setup is larger
303 since parallel orientation reduces diffusion by curling the electrons in the $x\text{-}y$
304 direction (see Equation 1.7) but for our relatively weak magnetic field and short
305 drift distance the difference is negligible.

306 1.3.2 Coordinate Systems and Dimensions

307 In order to describe events in our detector, we use three distinct spaces: the de-
308 tector space \mathcal{D} , the readout space \mathcal{R} and the pad space \mathcal{P} . Each space is later
309 used to represent ionization electrons at different stages of the detection process:
310 their creation in the gas, their final position when hitting the readout plane, and
311 finally their representation in the discrete pad space.

312 Detector Space

313 The detector space \mathcal{D} represents the physical space of our detector. We de-
314 scribe it using Cartesian coordinates (x, y, z) . The z -axis is the detector's axis of

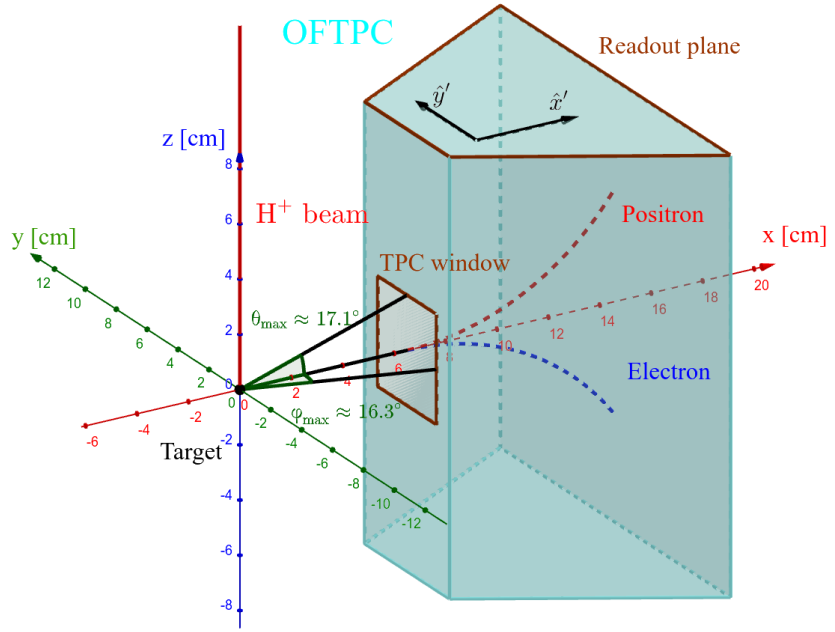


Figure 1.2: Schematics of the first sector OFTPC with detector space coordinates.

symmetry, with its negative direction aligned with the proton beam. The origin $(0, 0, 0)$ is located at the center of the irradiated target. The positive x -axis passes through the center of one the OFTPCs along the intersection of its two planes of symmetry. The y -axis is then chosen to maintain a right-handed coordinate system.

Since the detector has a hexagonal symmetry, we use only one of its sectors in this work – the first sector $\mathcal{D}_1 \subset \mathcal{D}$ which is defined by the condition:

$$(x, y, z) \in \mathcal{D}_1 \Leftrightarrow |y| \leq x \tan \frac{\pi}{6}. \quad (1.8)$$

Simulations in this sector can be applied to all sectors by rotating the coordinates accordingly. The volume of the OFTPC in this sector, which has the shape of a trapezoidal prism, has these boundaries:

$$x \in [x_{\min}, x_{\max}] = [6.51, 14.61] \text{ cm}, \quad (1.9)$$

$$z \in [z_{\min}, z_{\max}] = [-8, 8] \text{ cm}, \quad (1.10)$$

$$y_{\max}(x_{\min}) = -y_{\min}(x_{\min}) = 2.75 \text{ cm}, \quad (1.11)$$

$$y_{\max}(x_{\max}) = -y_{\min}(x_{\max}) = 7.45 \text{ cm}, \quad (1.12)$$

where $y_{\max}(x)$ is the maximal value of the y -coordinate for a given x . The readout is located at $z = 8$ cm; for some purposes, we also define the distance to the readout $d_r = 8 \text{ cm} - z$ as an alternative to the z -coordinate. Keeping this paragraph as it is because the OFTPC volume is distinct from the first sector and some parts of this thesis use the space beyond this volume.

We also use spherical coordinates (r, θ, φ) with θ measured relative to the xy plane.

332 **Readout Space**

333 The readout space \mathcal{R} represents the drift time and final positions of ionization
 334 electrons as measured by an ideal continuous readout. We describe it using
 335 coordinates (x', y', t) , where x' and y' correspond to the detector coordinates at
 336 the readout plane ($z = 8$ cm). Currently not entirely sure how to put this
 337 into a figure since only x' and y' correspond to the detector coordinates, it will
 338 make more sense when visualizing the map. The drift time t is approximately
 339 proportional to d_r .

340 **Pad Space**

341 The pad space \mathcal{P} represents the time bin and pad number of ionization electrons
 342 as measured by an ideal discrete readout. It is not really a subspace of \mathcal{R} but
 343 there is a mapping from \mathcal{R} to \mathcal{P} . It is a discretization of a part of \mathcal{R} , the mapping
 344 can be adjusted depending on the simulation. If we assume uniform electric field
 345 there will be gaps, we don't use gaps in the reconstruction since the electrons
 346 should be pulled towards the pads.

347 The readout of the OFTPC will consist (is the design final?) of 128 rectangular
 348 pads arranged in a staggered pattern. Parameters of the pad layout are shown in
 349 Figure 1.3.

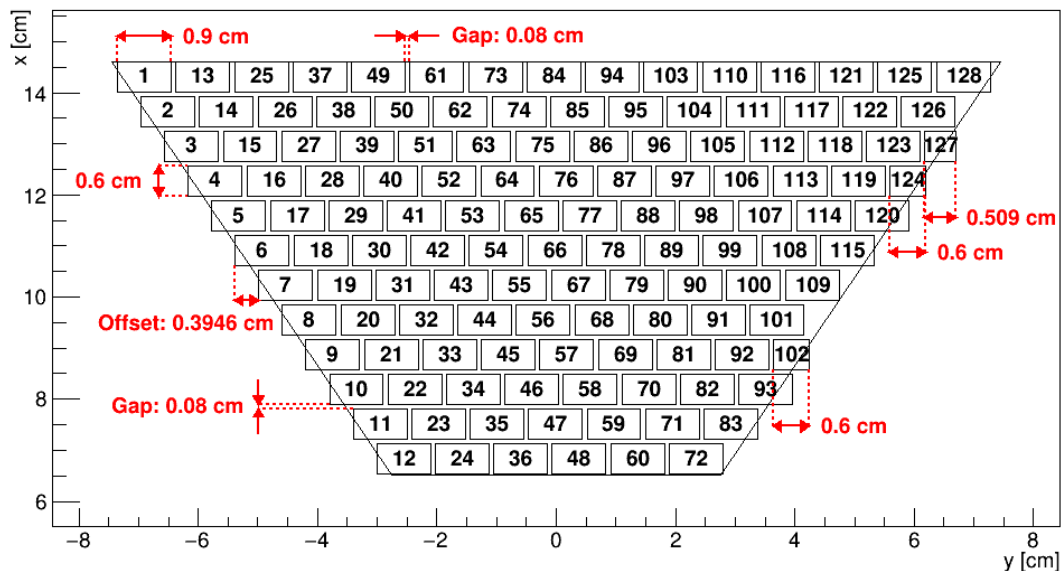


Figure 1.3: Pad layout of the OFTPC and its parameters.

350 **1.3.3 Magnetic Field Simulation**

351 The magnetic field inside our detector is produced by six permanent magnets. It
 352 was simulated using Ansys Maxwell ([citation?](#)) which gives us values on a regular
 353 grid. Visualization of the magnetic field is shown in Figure 1.4. Whenever we
 354 need to work with values outside this grid, we use trilinear interpolation described
 355 in Section 1.3.3 below.

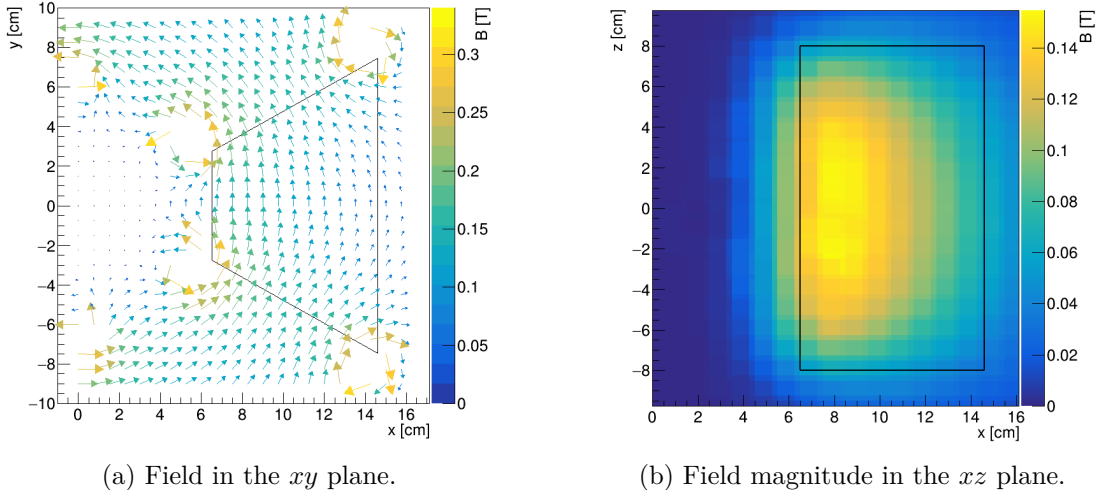


Figure 1.4: Magnetic field simulation results. OFTPC volume is marked with black lines.

356 Trilinear Interpolation

357 Trilinear interpolation is a 3D generalization of linear interpolation. It can be
 358 used to interpolate a function whose values are known on a regular grid with
 359 rectangular prism cells. We use this simple method for interpolating the magnetic
 360 field, and it is later used in Section 3.2.1 to interpolate the Ionization Electron
 361 Map, a key component of our track reconstruction algorithm. In both cases, we
 362 use a regular cubic grid (apparently it is also called a [Cartesian grid](#)).

363 Could put a paragraph about linear interpolation here if it is not clear from
 364 the equations below.

365 Let us consider a cell of our regular grid (a cube) with an edge of length a
 366 containing the point $\mathbf{C} = (x, y, z)$ where we want to interpolate a function
 367 $f: \mathbb{R}^3 \rightarrow \mathbb{R}$. We know the values of this function at the vertices of the cell
 368 $\mathbf{C}_{ijk} = (x_0 + ia, y_0 + ja, z_0 + ka)$, where $i, j, k \in \{0, 1\}$ are indices. We also define
 369 the points $\mathbf{C}_{ij} = (x, y_0 + ia, z_0 + ja)$ and $\mathbf{C}_i = (x, y, z_0 + ia)$. Then the interpolated
 370 value $\hat{f}(\mathbf{C})$ can be calculated as a composition of three linear interpolations (see
 371 Figure 1.5):

$$\hat{f}(\mathbf{C}_{ij}) = (1 - x_d) f(\mathbf{C}_{0ij}) + x_d f(\mathbf{C}_{1ij}), \quad (1.13)$$

$$\hat{f}(\mathbf{C}_i) = (1 - y_d) \hat{f}(\mathbf{C}_{0i}) + y_d \hat{f}(\mathbf{C}_{1i}), \quad (1.14)$$

$$\hat{f}(\mathbf{C}) = (1 - z_d) \hat{f}(\mathbf{C}_0) + z_d \hat{f}(\mathbf{C}_1), \quad (1.15)$$

372 where x_d , y_d , and z_d are given as follows:

$$x_d = \frac{x - x_0}{a}, \quad y_d = \frac{y - y_0}{a}, \quad z_d = \frac{z - z_0}{a}. \quad (1.16)$$

373 We can also write

$$\hat{f}(\mathbf{C}) = \sum_{i,j,k \in \{0,1\}} t_x^i t_y^j t_z^k f(\mathbf{C}_{ijk}), \quad (1.17)$$

$$t_\alpha \stackrel{\text{def}}{=} \begin{pmatrix} t_\alpha^0 \\ t_\alpha^1 \end{pmatrix} = \begin{pmatrix} 1 - \alpha_d \\ \alpha_d \end{pmatrix}, \quad (1.18)$$

³⁷⁴ where $\alpha \in \{x, y, z\}$ is an index. Furthermore, we can write $\hat{f}(\mathbf{C})$ as a polynomial:

$$\hat{f}(\mathbf{C}) = \sum_{\alpha, \beta, \gamma \in \{0,1\}} \sum_{i=0}^{\alpha} \sum_{j=0}^{\beta} \sum_{k=0}^{\gamma} (-1)^{(\alpha-i)+(\beta-j)+(\gamma-k)} f(\mathbf{C}_{ijk}) x_d^{\alpha} y_d^{\beta} z_d^{\gamma}. \quad (1.19)$$

³⁷⁵ We take advantage of this form when generalizing trilinear interpolation to irregular
³⁷⁶ grid in section 3.2.2.

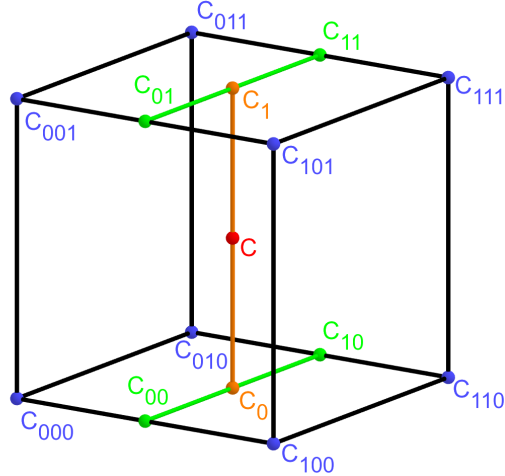


Figure 1.5: Visualization of trilinear interpolation as a composition of linear interpolations. Image drawn in GeoGebra and inspired by a similar image on Wikipedia (which looks a bit worse) – is credit necessary?

³⁷⁷ Maybe a citation here, although I am not sure it is necessary since it could
³⁷⁸ be considered common knowledge. The last two equations are my own. Maybe
³⁷⁹ x_0 , etc. should be explicitly described.

2. Track Simulation

In order to develop and test the reconstruction algorithm, electron and positron tracks are simulated inside the first sector \mathcal{D}_1 of our detector (see Section 1.3.2) with different initial parameters. Two approaches are currently used to simulate tracks, each of them for different purpose.

The **Microscopic Simulation** uses the Garfield++ toolkit [1]. Within this toolkit, the High Energy Electro-Dynamics (HEED) program [25] is used to simulate the primary particle and the class *AvalancheMicroscopic* to simulate the drift of secondary electrons created by ionization in the gas. This is the most precise and time-consuming simulation used; our current goal is to be able to successfully reconstruct its results and determine our best-case energy resolution.

The **Runge-Kutta Simulation** uses the 4th order Runge-Kutta numerical integration ([add citation for Runge-Kutta](#)) to simulate the trajectory of the primary particle in the electromagnetic field inside the detector. It is relatively fast since it does not simulate the secondary particles. It is used as part of our reconstruction algorithm and for testing some parts of the reconstruction.

All of these simulations require the knowledge of the electromagnetic field inside the detector. A uniform electric field of $400 \text{ V}\cdot\text{cm}^{-1}$ is assumed. The magnetic field was simulated in Maxwell (see Section 1.3.3). [add citation](#)

[Single track in positive x direction or initial parameter randomization. Importance of gas composition, used gas compositions.](#)

2.1 Microscopic Simulation

The microscopic simulation, the most detailed simulation used in this work, is performed using the Garfield++ toolkit [1].

The electron transport properties are simulated using the program Magboltz ([Add citation](#)). Two different gas mixtures were used: 90% Ar + 10% CO₂ and 70% Ar + 30% CO₂. The second mixture will be used in our detector. The temperature is set to 20 °C, the pressure is atmospheric.

The primary track is simulated using the program HEED [25], which is an implementation of the photo-absorption ionization model. This program provides the parameters of ionizing collisions. HEED can also be used to simulate the transport of delta electrons; we do not account for these in the current simulation but plan to include them in the future. The photons created in the atomic relaxation cascade ([fluorescence reabsorption, ?](#)) are also not simulated.

Finally, we use the microscopic tracking provided by the class *AvalancheMicroscopic* to simulate the drift of the ionization electrons. Each electron is followed from collision to collision using the equation of motion and the collision rates calculated by Magboltz.

[First simulated track in the z direction should be described in detail here \(own subsection?\). Figures.](#)

[Add more detailed and better description of HEED, and microscopic tracking \(each their own subsection?\). Could also mention Monte Carlo \(requires gas file generation - Magboltz\) and Runge-Kutta simulation implemented in Garfield,](#)

423 why we don't use them (another subsection? rename the section to Garfield++
424 simulation and mention all relevant parts?).

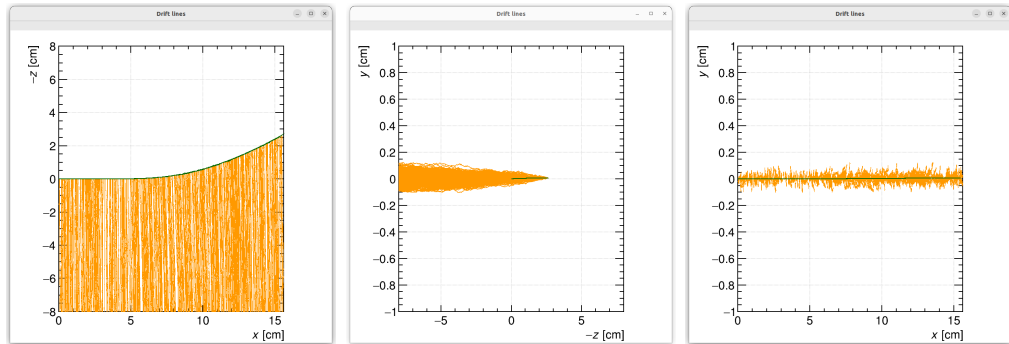


Figure 2.1: Example of a simulated electron track in 70 % argon and 30 % CO₂ atmosphere (on the left). Swap for better images, better zoom. Explain drift lines, primary particle.

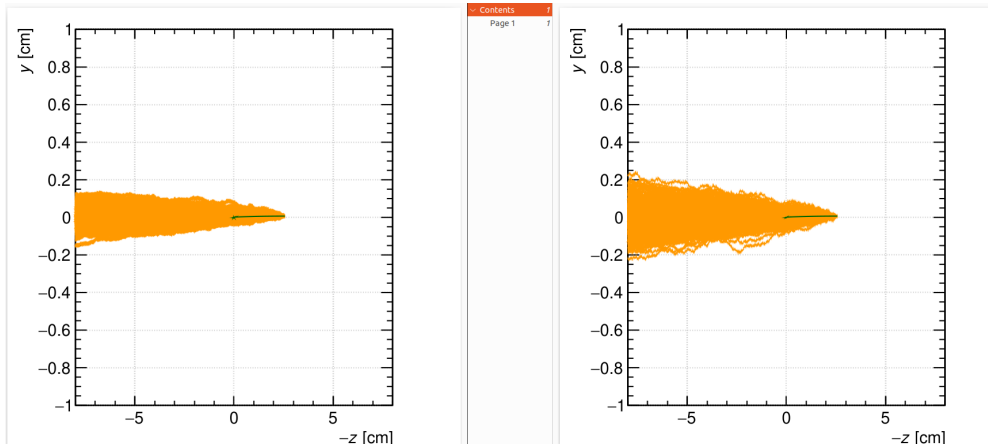


Figure 2.2: Comparison of diffusion in a simulated electron track in 70 % argon, 30 % CO₂ atmosphere and in 90 % argon, 10 % CO₂ atmosphere (on the right). Swap for better image, better zoom. Or put the same pictures for both comparisons in one subfigure, etc. Describe better.

425 2.2 Runge-Kutta Simulation

426 Trajectory simulation with 4th order Runge-Kutta. Relativistic equation that is
427 numerically integrated by the algorithm.

3. Track Reconstruction

In the first stage of the reconstruction algorithm, we reconstruct the track of a primary particle (either an electron or a positron). The result of this step is then used to determine the energy of the particle (Section 4).

The **Reconstruction Assuming Steady Drift** uses the standard TPC approach. With parallel fields, the drift inside a uniform electric field remains undistorted (reference to some future part of the TPC chapter). Therefore, we only need to reconstruct the z -coordinate from the drift time using the known drift velocity. We also assume that the readout coordinates (x', y', t) are known exactly, neglecting the pads and time bins.

Reconstruction using the **Ionization Electron Map** (from now on referred to as *the map*) uses a simulation of the drift of secondary (ionization) electrons within the detector volume. This simulation can then be used to interpolate the initial position of the secondary electrons. First attempts neglect the pads.

We use the map for reconstruction in two different ways. The first one uses gradient descent search along with trilinear interpolation (see Section 1.3.3) of the map. The second method uses interpolation on the irregular inverse grid with a linear polynomial.

The **Discrete Reconstruction** uses the map; instead of reconstructing the exact position of each electron, we reconstruct the center of each hit pad with the time corresponding to the midpoint of the time bin. The electron count in each TPC bin (consisting of the pad and the time bin) serves as the charge value, which is then used as a weight in the energy reconstruction fit.

3.1 Reconstruction Assuming Steady Drift

As the first step, we decided to try to reconstruct an electron track with a special set of initial parameters. The origin of the particle is given by the origin of our coordinate system. The initial direction is given by the positive x -axis. This means the magnetic field of our detector is perpendicular to the momentum of the particle at all times, and we can reduce the problem to two-dimensional space. As an example, we use a track simulated using the microscopic simulation (see Section 2.1) with a kinetic energy of 8 MeV. The gas composition used in this simulation is 90% Ar + 10% CO₂. Might be better to describe this track in Section 2.1.

In this approach to the reconstruction of the track, we decided to use the common method used in a standard TPC. This will allow us to explore the significance of the atypical behavior in our OFTPC. Additionally, we assume the readout is continuous to further simplify the problem. In this approximation, we reconstruct the initial position of each ionization electron.

The reconstruction is then defined by the following relations between the coordinates of the detector space and the readout space (see Section 1.3.2):

$$x = x', \quad (3.1)$$

$$y = y', \quad (3.2)$$

$$z = v_d t, \quad (3.3)$$

468 where v_d is the drift velocity of electrons in the given gas mixture. At a phe-
 469 nomenological level, this velocity can be considered as a function of the electric
 470 field \mathbf{E} and the magnetic field \mathbf{B} :

$$v_d = v_d(\mathbf{E}, \mathbf{B}). \quad (3.4)$$

471 Equation taken from Garfield user manual. The Garfield++ toolkit uses this
 472 fact to accelerate their drift simulation with non-microscopic approaches (could
 473 mention in the simulation chapter). Since we assume a uniform electric field in
 474 our detector and we want to neglect the effect of our unusual magnetic field, we
 475 consider the drift velocity to be constant in this scenario. We then approximate
 476 this velocity by fitting the dependence $z(t)$ taken from the simulated ionization
 477 electrons. This is in one of the provisional figures. Also, this description is
 478 not completely accurate; in reality, we fit $t1:8-y0$ with $a1*x+a0$ and then invert
 479 this and use $8-y0 = b1*t1+b0$ (old coordinates); $b1=1/a1$ functions as the drift
 480 velocity. Maybe also define this 8-z variable as an alternative to z in Section 1.3.2
 481 and then use it when correcting this.

482 Later, in a commit after this, I plotted some residues (provisional figure),
 483 which could be useful, but for some reason they are residuals from a spline fit of
 484 the track?! Probably redo this without the spline fit; just explore the difference
 485 in individual points.

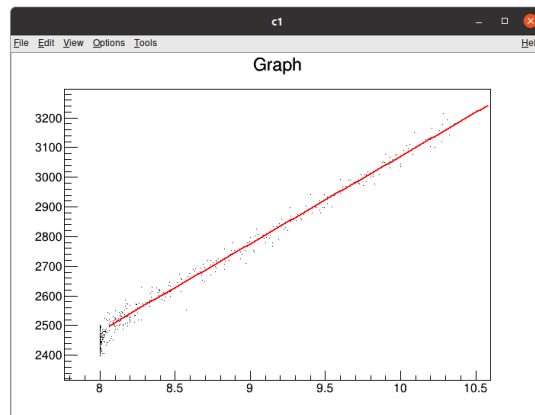


Figure 3.1: Dependence of the drift time on the z coordinate in 90 % argon and 10 % CO₂ atmosphere, fitted with a linear function. The fitted function gives us the average drift velocity in the gas and can be used for rough reconstruction in our TPC. Swap for better image with axis labels, etc. Maybe write the fitted equation.

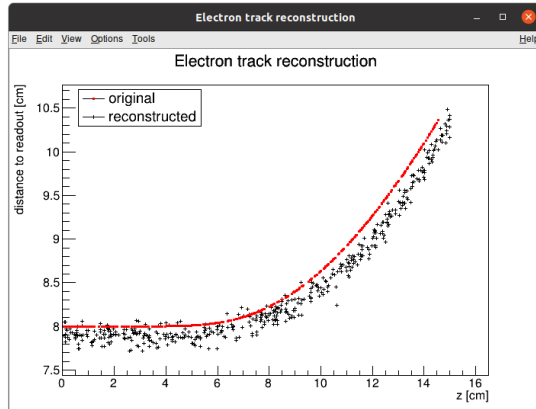


Figure 3.2: First attempt at a track reconstruction using only the drift velocity. This approach works well in a standard TPC (ideally cite some source?). 90 % argon and 10 % CO₂ atmosphere. Swap for better image, correct coordinates.

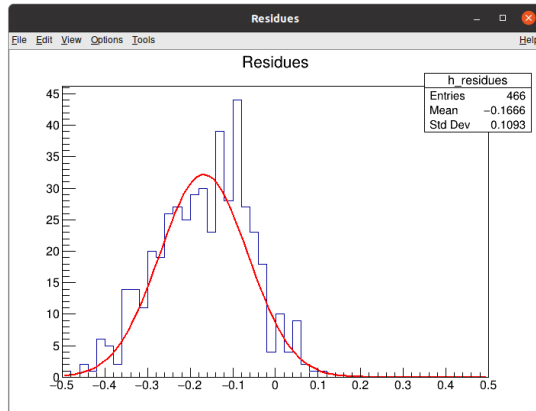


Figure 3.3: First attempt at a track reconstruction using only the drift velocity, residues. Swap for better image, correct coordinates. What's causing the shift? Explain details.

486 3.2 Ionization Electron Map

487 Inside an OFTPC, the drift of the secondary (ionization) electrons is significantly
 488 affected by its magnetic field (pictures of the distortion later, the effect is bigger
 489 for the 90/10 composition.). We need to take this into account for accurate
 490 reconstruction. In the first approximation, we assume a continuous readout (i.e.,
 491 we neglect pads). We can then reconstruct the original position of each ionization
 492 electron using its readout coordinates. For this purpose, we use the ionization
 493 electron map.

494 The ionization electron map represents a mapping from the detector space
 495 to the readout space (see Section 1.3.2). It tells us what readout coordinates
 496 (x', y', t) we can expect on average for an ionization electron created at the detec-
 497 tor coordinates (x, y, z). More precisely it is a mapping to the distributions on
 498 the readout space; we can simplify this as only the means $\bar{\mathcal{M}}$ and the covariance

499 matrices \mathcal{M}_{cov} , assuming Gaussian distribution.

$$\mathcal{M} : \mathcal{D} \longrightarrow \mathcal{R}, (x, y, z) \longmapsto (x', y', t). \quad (3.5)$$

500 To get an approximation of this mapping, we simulate the drift of ionization
 501 electrons generated on a regular grid inside the volume of our OFTPC ¹. It
 502 is also useful to simulate multiple (100 in our case) electrons originating from
 503 the same position so we can get a better information about the average drift
 504 and its variance. In order to get more accurate results, we use the microscopic
 505 simulation of these electrons described in Section 2.1. When evaluating the map
 506 inside the grid, we use trilinear interpolation (see Section 1.3.3). From now on,
 507 we will denote this interpolated simulation with the same symbol \mathcal{M} .

508 Finally, we need to invert the map to get the original detector coordinates
 509 (x, y, z) for the given readout coordinates (x', y', t) . In our case, we can reasonably
 510 assume that the mapping $\overline{\mathcal{M}}$ is one-to-one (as seen in the simulations). We
 511 implemented two methods for this purpose: the gradient descent search (Section
 512 3.2.1) and interpolation on the inverse grid (Section 3.2.2).

513 The simulation of the map is a computationally heavy task. For this reason,
 514 we use the MetaCentrum grid [3] to parallelize needed calculations. At first, this
 515 was done by evenly distributing the simulated electrons across the individual jobs
 516 in a simulation with only one electron per vertex in the regular grid with a spacing
 517 of one centimeter.

518 Later, a more efficient approach was implemented, accounting for the varying
 519 lengths of the drift of individual electrons. If we index the electrons in the order
 520 of increasing coordinates y, x, z ([picture?](#)), we can express the number n_l of full
 521 XY layers (i.e., electrons with the same z coordinate) of electrons with index less
 522 than or equal to i

$$n_l(i) = \left\lfloor \frac{i}{n_{xy}} \right\rfloor, \quad (3.6)$$

523 where n_{xy} is the number of electrons in each XY layer calculated simply by counting
 524 the electrons that satisfy boundary conditions for x and y . **These conditions**
 525 **should be mentioned above; sector condition + maximal x value.** The number of
 526 electrons remaining in the top layer is then

$$n_r(i) = i \bmod n_{xy}. \quad (3.7)$$

527 Finally, we can calculate the sum of the drift gaps of electrons up to index i

$$d_{\text{sum}} = (z_{\max} - z_{\min})n_{xy}n_l - \frac{n_l(n_l - 1)}{2}n_{xy}l + n_r(z_{\max} - z_{\min} - n_l l). \quad (3.8)$$

528 We then use a binary search algorithm to find the maximum index i such that
 529 the value of this sum is less than the fraction $\frac{\text{job id}}{\max \text{ job id}}$ of the total sum. This way
 530 we obtain the minimal and the maximal index of electrons simulated in the given
 531 job. **The spacing l should be probably defined above + picture of the simulating**
 532 **grid (1 layer). zmin zmax also**

533 After the simulation of the map, we calculate the mean readout coordinates
 534 assuming Gaussian distribution (i.e., we use averages). We also calculate standard

¹we do not take the detector walls into account and simulate even outside of the OFTPC which lets us interpolate even close to the walls

535 deviations in a later commit, should be upgraded to the covariance matrix. We
536 never actually plotted the distributions we get when simulating the same electron
537 multiple times, so we do not know if our assumptions are accurate (could also
538 run some statistical test to see how well the Gaussian distribution fits).

539 The obtained map is then stored in a custom class template *Field*, could
540 expand on that. Maybe earlier, since the same template is used for the magnetic
541 field.

542 Could insert a table here describing all 4 simulations of the map (gas composi-
543 tion, spacing, etc.). Simulation inside of one sector (at first double angle). Extra
544 space on the sensor. Edge cases not taken into account (TPC wall). Using qsub
545 (not sure if important). Add plots of distortion of the coordinates. Could also do
546 these plots in a different way (e.g., drawing all the endpoints of each ionization
547 electron or some error ellipse plot).

548

549 Images to add (comparison of both simulations):

- 550 • 3D visualization of the map, simulation example
- 551 • z vs. t plot
- 552 • XY plane distortion for different z values; with arrows and error bars, for
553 all z -layers with different colors
- 554 • XZ plane ($y = 0$) distortion in x (maybe not necessary?)
- 555 • XT plot ($y = 0$) showing (small) distortion in drift times

556

557 More images:

- 558 • Residuals of the continuous readout reconstruction.

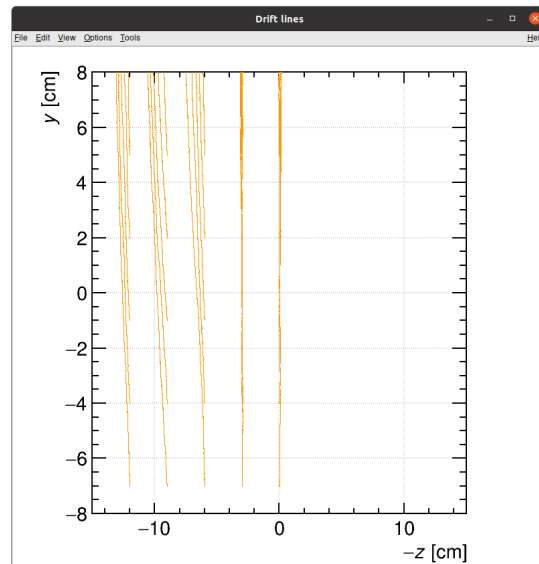


Figure 3.4: Example of map generation. Swap for better image, correct coordinates.

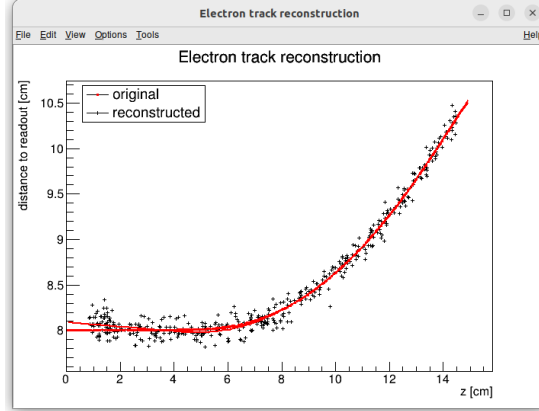


Figure 3.5: Example reconstruction with the map. Swap for better image, correct coordinates.

559 3.2.1 Gradient Descent Search

560 The first implemented method of reconstruction uses a gradient descent search
 561 to calculate an inversion of the map $\bar{\mathcal{M}}$ in a given point. Gradient descent is
 562 an iterative minimization algorithm for multivariate functions. Let $R \in \mathcal{R}$ be
 563 a point in the readout space; we want to find a point $D = (x, y, z) \in \mathcal{D}$ in
 564 the detector space such that

$$565 \quad \bar{\mathcal{M}}(D) = R = (x'_R, y'_R, t_R). \quad (3.9)$$

566 We define a function f_R in the readout space as a distance in this space:

$$567 \quad f_R(x', y', t) = \sqrt{(x' - x'_R)^2 + (y' - y'_R)^2 + v_d^2(t - t_R)^2}, \quad (3.10)$$

568 where v_d is an approximation of the drift velocity in the TPC, obtained from
 569 the reconstruction in Section 3.1 (there will be an image with the linear fit there).
 570 We make an initial guess (actually in the original code we just take $z = 0$):

$$571 \quad D_0 = (x'_R, y'_R, v_d t). \quad (3.11)$$

572 Assuming we have the n -th estimate D_n , we calculate the i -th component of
 573 the gradient of $f_R \circ \bar{\mathcal{M}}$ numerically using central differences:

$$574 \quad [\nabla(f_R \circ \bar{\mathcal{M}})]^i(D_n) \approx \frac{f_R(\bar{\mathcal{M}}(D_n + s \cdot e^i)) - f_R(\bar{\mathcal{M}}(D_n - s \cdot e^i))}{2s}, \quad (3.12)$$

575 where $e^i \in \mathcal{D}$ is the i -th coordinate vector and s is the step size. The step size
 576 should be sufficiently small; initially, we set it as a fraction of the map's grid
 577 spacing $s = \frac{l}{10}$. During the minimization, we check that $f_R(\bar{\mathcal{M}}(D_n)) < 10s$
 578 at all times. When using trilinear interpolation, it would be more efficient to
 579 calculate the gradient explicitly (\pm same result). This could be implemented
 580 inside the *Field* template class. The next iteration can be calculated as follows:

$$581 \quad D_{n+1} = D_n - \gamma \nabla(f_R \circ \bar{\mathcal{M}})(D_n), \quad (3.13)$$

582 where $\gamma \in \mathbb{R}^+$ is the damping coefficient. It should be set to a small enough
 583 value to ensure convergence, but large enough for sufficient converging speed.

579 The minimization stops either when the error $f_R(\bar{\mathcal{M}}(D_n))$ drops below a specified
 580 value or when the number of iterations exceeds a certain limit (in this case,
 581 a message is printed into the console). The parameters of this method can be
 582 further optimized (e.g., a better choice of γ , gradient computation); instead, we
 583 later decided to use the interpolation on the inverse grid described in the next
 584 section.

585 Measure reconstruction duration and compare it with the inverse grid inter-
 586 polation? Also compare the result? Not sure if this has to be cited.

587 3.2.2 Interpolation on the Inverse Grid

588 Interpolating between known points in the readout space. Gaussian elimina-
 589 tion, multivariate polynomial. Benefits compared to the gradient descent search
 590 method (one-time computation for the whole map is easy to achieve if needed).

591 The currently used baseline reconstruction method is the interpolation on
 592 the inverse grid. Rather than attempting to invert the trilinearly interpolated
 593 map as in the previous section, we take advantage of the fact that the map $\bar{\mathcal{M}}$
 594 is one-to-one (isomorphism is supposed to preserve structure, not sure how to
 595 interpret that here). Since we have simulated values of this map on a regular
 596 grid in the detector space \mathcal{D} , we also know the inverse map $\bar{\mathcal{M}}^{-1}$ on the irregular
 597 inverse grid in the readout space \mathcal{R} . To get an approximation of the inverse map
 598 in the entire readout space, we can use interpolation.

599 Since the inverse grid is irregular, trilinear interpolation cannot be applied.
 600 Given that the simulated map is dense enough to provide a good approxima-
 601 tion considering the size of our pads, we can adopt a similar approach (more
 602 complicated and computationally heavy alternative would be natural neighbor
 603 interpolation). As shown in Equation 1.19 in Section 1.3.3, trilinear interpolation
 604 can be expressed as a polynomial:

$$\hat{f}(x, y, z) = axyz + bxy + cxz + dyz + ex + fy + gz + h, \quad (3.14)$$

605 where a, b, c, d, e, f, g, h are coefficients uniquely determined by the values of
 606 the function at the vertices of the interpolation cell. We can generalize this
 607 for a function defined on an irregular grid. Given the function values at any eight
 608 points, we can write a system of eight linear equations

$$\begin{pmatrix} x_1y_1z_1 & x_1y_1 & x_1z_1 & y_1z_1 & x_1 & y_1 & z_1 & 1 \\ \vdots & \vdots \\ x_8y_8z_8 & x_8y_8 & x_8z_8 & y_8z_8 & x_8 & y_8 & z_8 & 1 \end{pmatrix} \begin{pmatrix} a \\ \vdots \\ h \end{pmatrix} = \begin{pmatrix} f(x_1, y_1, z_1) \\ \vdots \\ f(x_8, y_8, z_8) \end{pmatrix}, \quad (3.15)$$

609 which has a unique solution for the coefficients for most values of (x_n, y_n, z_n) and
 610 $f(x_n, y_n, z_n)$, where $n \in \{1, \dots, 8\}$.

611 This approach introduces a small complication: finding the correct pseudocell
 612 (i.e., the image of eight vertices forming a cubic cell in the regular grid) in
 613 the inverse grid. The eight irregularly spaced vertices of this pseudocell do not
 614 define a unique volume, so there are multiple possible ways to partition \mathcal{R} into
 615 pseudocells, with no obvious choice among them.

616 We are currently ignoring this problem and performing binary search along
 617 x, y, z (in this order). It shouldn't matter too much because the 70/30 map

618 doesn't cause such a big distortion and was even accidentally extrapolated for all
 619 z different from the central plane. Interpolation should be generally faster than
 620 the gradient descent since we don't need to iterate. We also don't need to optimize
 621 it to improve performance, if it's too slow we can even calculate the coefficients
 622 for the entire map before reconstruction.

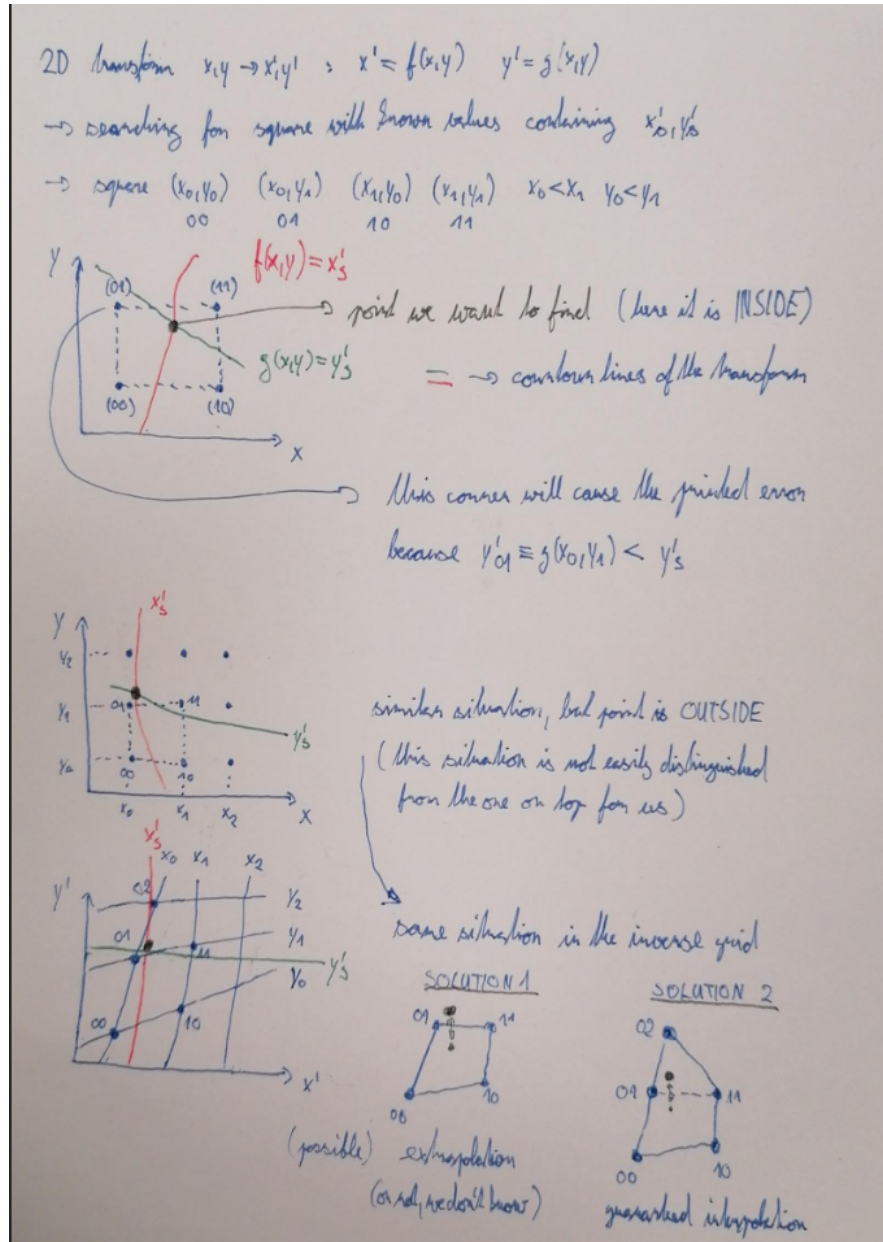


Figure 3.6: Selection of the points for interpolation. Create better images; use the explanation interpolation vs. extrapolation strange property. Solution 2 probably does not make much sense.

623 3.3 Discrete Reconstruction

624 Reconstruction with pads and time bins. Maybe testing different pads. Mapping
 625 the center of the pad (along with the midpoint of the time bin) isn't necessarily

626 the best approach since it might not correspond to the average parameters of
627 an electron with these readout parameters (insignificant?).

628 It is also possible to make this a subsection of the map, making the previous
629 subsections parts of a new subsection 'Map Inversion'

630 4. Energy Reconstruction

631 The second stage is the reconstruction of the particle's energy using a fit of its
632 reconstructed track (see Section 3). We have tested three ways of reconstructing
633 the energy. Fitting is done using the MINUIT algorithm implemented in
634 ROOT [2]. **Cite some CERN article directly on MINUIT, can add a section.**

635 The **Cubic Spline Fit** is a tested and later rejected method of energy reconstruction. It uses smoothly connected piecewise cubic polynomials between
636 uniformly spaced nodes. Energy is calculated using the fit parameters by computing
637 the radius of curvature in different points of the fitted curve using the known
638 magnitude of the magnetic field perpendicular to the trajectory. We rejected this
639 method because tuning of the fit to have a reasonably stable radius of curvature
640 turned out to be unpractical.

641 The **Circle and Lines Fit** was chosen as an alternative since this corresponds to the shape of a trajectory of a charged particle crossing a finite volume
642 with a homogeneous magnetic field. The energy of the particle can be estimated
643 using the fitted radius and the magnitude of the perpendicular magnetic field in
644 the middle of the TPC.

645 The **Runge-Kutta Fit** uses the 4th order Runge-Kutta numerical integration
646 described in Section 2.2. Initial parameters of the track (including the particle's
647 energy) are optimized so that the integrated trajectory fits to the reconstructed
648 one. This fit can also be performed as a single parameter (i.e., energy) fit if we
649 get the initial position and orientation of the particle on the entrance to the TPC
650 from previous detectors (Tpx3 and MWPC, see Section 0.2).

653 4.1 Cubic Spline Fit

654 The first attempt to get an early estimate of the kinetic energy of the particle
655 uses a cubic spline fit. We use an electron track starting in the origin of our
656 coordinate system with an initial direction in the positive x axis. The example
657 track is simulated microscopically (see Section 2.1) with a kinetic energy of 8 MeV
658 in a gas mixture 90% Ar + 10% CO₂ (the same track was used in Section 3.1).
659 **This track should probably be described in the simulation chapter.**

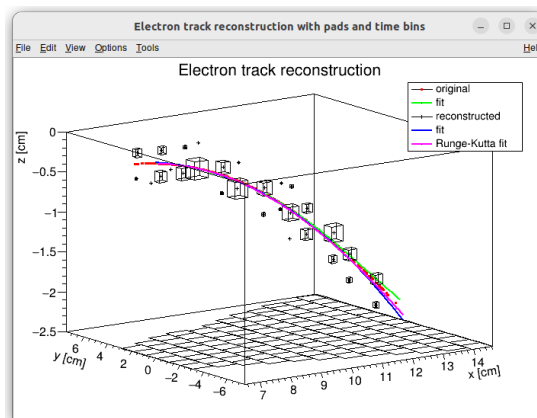


Figure 4.1: Example of a fitted reconstructed track. **Swap for better image.**

660 In order to calculate the spline, we use the class *TSpline3* from ROOT. This
 661 allows us to evaluate the spline using the coordinates (x_n, z_n) of each node and
 662 the derivatives d_1, d_2 in the first and the last node. We can fit these parameters
 663 of a fixed amount of nodes to the simulated trajectory. We use the IMPROVE
 664 algorithm provided by the *TMinuit* class in ROOT. This algorithm attempts to
 665 find a better local minimum after converging.

666 After the fit, we want to get an energy estimate. In order to calculate it, we
 667 need the radius of curvature, which we get from the fitted spline at every point
 668 of the trajectory. The part of the spline corresponding to a given node is defined
 669 as

$$z(x) = z_n + b\Delta x + c(\Delta x)^2 + d(\Delta x)^3, \quad (4.1)$$

670 where $\Delta x = x - x_n$ and b, c, d are coefficients. Using this equation, we derive
 671 the radius of curvature¹ as:

$$r(x) = \frac{(1 + z'^2(x))^{\frac{3}{2}}}{z''(x)} = \frac{(1 + (b + 2c\Delta x + 3d(\Delta x)^2)^2)^{\frac{3}{2}}}{2c + 6d\Delta x}. \quad (4.2)$$

672 Based on the geometry of the detector, we can assume the magnetic field
 673 $\mathbf{B}(x, 0, z) = (0, B(x, z), 0)$ for a track in the XZ plane. Since the electron is rela-
 674 tivistic, the effect of the electric field on its trajectory is negligible. The Lorentz
 675 force \mathbf{F}_L is then always perpendicular to the momentum of the electron and acts
 676 as a centripetal force \mathbf{F}_c :

$$\mathbf{F}_L = \mathbf{F}_c, \quad (4.3)$$

$$\|e\mathbf{v} \times \mathbf{B}\| = \frac{\gamma m_e v^2}{r}, \quad (4.4)$$

$$ec\beta B = \frac{E_{0e}\beta^2}{r\sqrt{1 - \beta^2}}, \quad (4.5)$$

$$\sqrt{1 - \beta^2} = \frac{E_{0e}\beta}{ecBr}, \quad (4.6)$$

677

$$\beta^2(x) = \left[1 + \left(\frac{E_{0e}}{ecB(x, z(x))r(x)} \right)^2 \right]^{-1}, \quad (4.7)$$

678 where e is the elementary charge, c is the speed of light in vacuum, m_e is the rest
 679 mass of electron, $E_{0e} = m_e c^2$ is the corresponding energy, γ is the Lorentz factor,
 680 \mathbf{v} is the velocity of the electron, and $\beta = \frac{v}{c}$. We can then finally get our estimate
 681 of the kinetic energy for a given point on the trajectory as follows:

$$E_{\text{kin}}(x) = \left(\frac{1}{\sqrt{1 - \beta^2(x)}} - 1 \right) E_{0e}. \quad (4.8)$$

682 We can then average these estimates at multiple points to get one final estimate.
 683 This method was later rejected in favor of the circle and lines fit described in
 684 Section 4.2. **Add some figures.**

¹For the general formula see https://en.wikipedia.org/wiki/Curvature#Graph_of_a_function

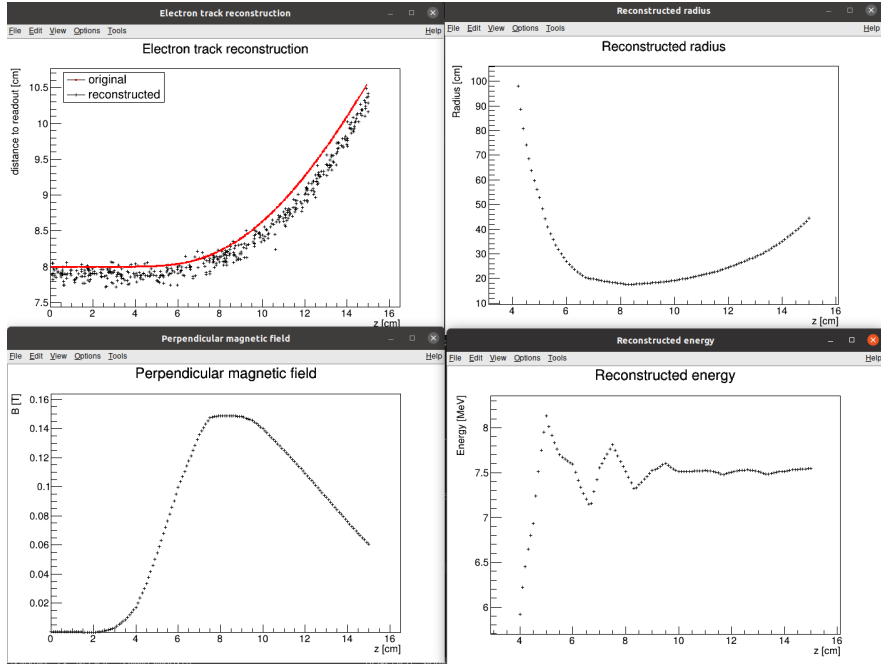


Figure 4.2: First attempt at a track reconstruction using only the drift velocity. Spline energy reconstruction attempt. Swap for better image(s) – subfigure environment, correct coordinates.

685 4.2 Circle and Lines Fit

686 Another way to estimate the particle's kinetic energy is to fit its trajectory with
 687 a circular arc with lines attached smoothly. This shape of trajectory corresponds
 688 to a movement of a charged particle through a homogeneous magnetic field per-
 689 pendicular to the particle's momentum and limited to a certain volume. In gen-
 690 eral, the shape of such a trajectory in a non-perpendicularly oriented field is
 691 a spiral. In our case, this component is negligible since the field is approxi-
 692 mately toroidal and the particle motion is nearly perpendicular to it. At first, we tested
 693 a 2D version of this fit, then we adapted it to 3D.

694 Our field is not homogeneous, it is therefore not entirely clear what value of
 695 magnetic field should be used along with the fitted radius (using equations 4.7
 696 and 4.8) to get the best estimate for the kinetic energy. Since we only use this
 697 method as the first iteration of the particle's energy that we later refine, an op-
 698 timal solution of this problem is not required. Instead, we tested two options:
 699 taking the value of the field in the middle of the fitted circular arc and taking
 700 the average field along it. We haven't really tried to plot this for multiple tracks,
 701 but these estimates are saved somewhere and could be plotted.

702 4.2.1 Two-dimensional fit

703 In the 2D case, the fitted function used for the electron track² described in Sec-
 704 tion 4.1 is defined as follows: Maybe describe this track that we used at the be-
 705 ginning somewhere earlier (section microscopic simulations → Testing track?) so
 706 that it is easier to refer to it in multiple sections. It is not part of the early GitHub

²Electron tracks bend towards negative z , we need to use the upper part of the circle

707 commits, so maybe it won't be possible to create exact replicas of the images,
 708 but they should be at least very similar.

$$z(x) = \begin{cases} a_1x + b_1 & x < x_1 \\ z_0 + \sqrt{r^2 - (x - x_0)^2} & x_1 \leq x \leq x_2 \\ a_2x + b_2 & x > x_2 \end{cases}, \quad (4.9)$$

709 where $a_{1,2}$ and $b_{1,2}$ are the parameters of the lines, (x_0, z_0) is the center of the cir-
 710 cle, r is its radius, and $(x_{1,2}, z_{1,2})$ are the coordinates of the function's nodes.
 711 That means we have 9 parameters ($z_{1,2}$ are not used in the function) along with
 712 2 continuity conditions and 2 smoothness conditions. For the fit, we use the co-
 713 ordinates of the nodes and the radius of the circle, which gives us 5 independent
 714 parameters (only the radius has to be larger than half of the distance between
 715 nodes). The continuity conditions (combined with the relations for $z_{1,2}$) are as
 716 follows:

$$z_{1,2} = a_{1,2}x_{1,2} + b_{1,2} = z_0 - \sqrt{r^2 - (x_{1,2} - x_0)^2}. \quad (4.10)$$

717 The smoothness conditions are as follows:

$$a_{1,2} = \frac{x_0 - x_{1,2}}{\sqrt{r^2 - (x_{1,2} - x_0)^2}}. \quad (4.11)$$

718 Equation 4.10 gives us the values of $b_{1,2}$

$$b_{1,2} = z_{1,2} - a_{1,2}x_{1,2}. \quad (4.12)$$

719 For the coordinates of the center of the circle, we can use the fact that the center
 720 has to lie on the axis of its chord. In other words, there is a value of a parameter t
 721 such that, using the parametric equation of the axis

$$\begin{pmatrix} x_0 \\ z_0 \end{pmatrix} = \begin{pmatrix} \frac{x_1+x_2}{2} \\ \frac{z_1+z_2}{2} \end{pmatrix} + t \begin{pmatrix} \frac{z_2-z_1}{2} \\ \frac{x_1-x_2}{2} \end{pmatrix}. \quad (4.13)$$

722 At the same time, the center has to be in a distance of r from the nodes:

$$(x_1 - x_0)^2 + (z_1 - z_0)^2 = r^2, \quad (4.14)$$

$$\left(\frac{x_1 - x_2}{2} + \frac{z_1 - z_2}{2} t \right)^2 + \left(\frac{z_1 - z_2}{2} + \frac{x_2 - x_1}{2} t \right)^2 = r^2, \quad (4.15)$$

$$\left(\left(\frac{x_2 - x_1}{2} \right)^2 + \left(\frac{z_2 - z_1}{2} \right)^2 \right) t^2 + \left(\frac{x_2 - x_1}{2} \right)^2 + \left(\frac{z_2 - z_1}{2} \right)^2 - r^2 = 0. \quad (4.16)$$

723 Since our electron track bends towards negative z and $x_2 > x_1$, we only care
 724 about the solution with $t > 0$

$$t = \sqrt{\frac{r^2}{\left(\frac{x_2 - x_1}{2} \right)^2 + \left(\frac{z_2 - z_1}{2} \right)^2} - 1}, \quad (4.17)$$

725

$$x_0 = \frac{x_1 + x_2}{2} + \frac{z_2 - z_1}{2} \sqrt{\frac{r^2}{\left(\frac{x_2 - x_1}{2} \right)^2 + \left(\frac{z_2 - z_1}{2} \right)^2} - 1}, \quad (4.18)$$

$$z_0 = \frac{z_1 + z_2}{2} - \frac{x_2 - x_1}{2} \sqrt{\frac{r^2}{\left(\frac{x_2 - x_1}{2} \right)^2 + \left(\frac{z_2 - z_1}{2} \right)^2} - 1}. \quad (4.19)$$

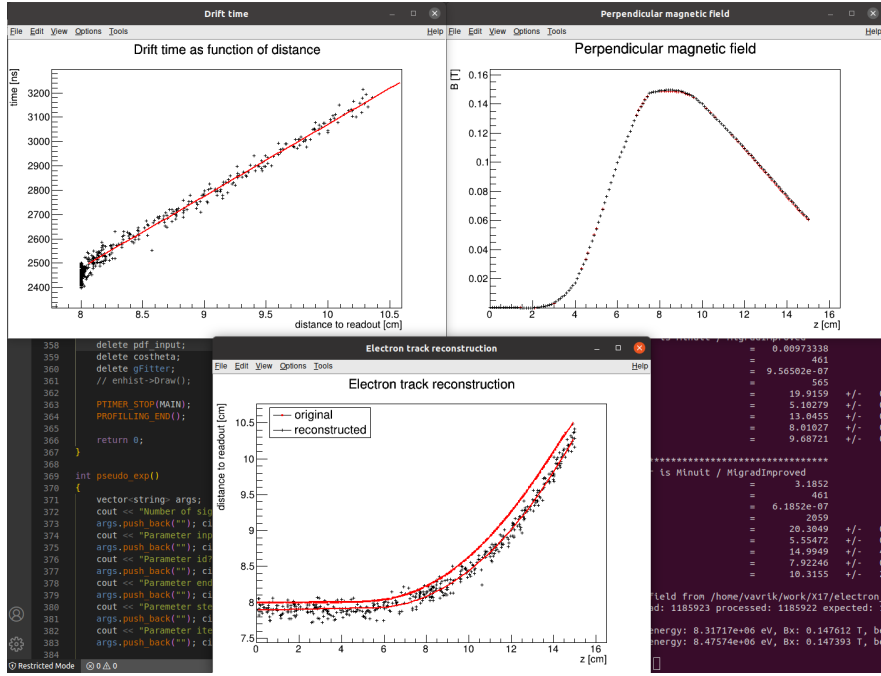


Figure 4.3: First attempt at a track reconstruction using only the drift velocity. Circle and Lines Fit in 2D. Swap for better image, correct coordinates.

726 The function defined in Equation 4.9 along with equations 4.11, 4.12, 4.18 and 4.19
 727 derived using the continuity and smoothness conditions (combined with the re-
 728 lations for $z_{1,2}$) fully define our fitted function with parameters $r, x_{1,2}, z_{1,2}$. Some
 729 pictures of the fit on the tested track. Results of the fit. Again, the actual fit
 730 uses $8-z$. Use GeoGebra schematics to generate a picture of 2D geometry.

731 Tested on a Runge-Kutta sample, and with microscopic tracks + map sim-
 732 ulation. Preliminary 2D version (done) and complete 3D version. Geometry of
 733 the fit with its derivation.

734 4.2.2 Three-dimensional fit

735 Explain the geometry and least square method used for the 3D fit.

736 4.3 Runge-Kutta Fit

737 Single parameter fit with 4th order Runge-Kutta simulated track. Future testing
 738 with microscopic simulations and map simulation. Derivation of the geometry
 739 (least squares).

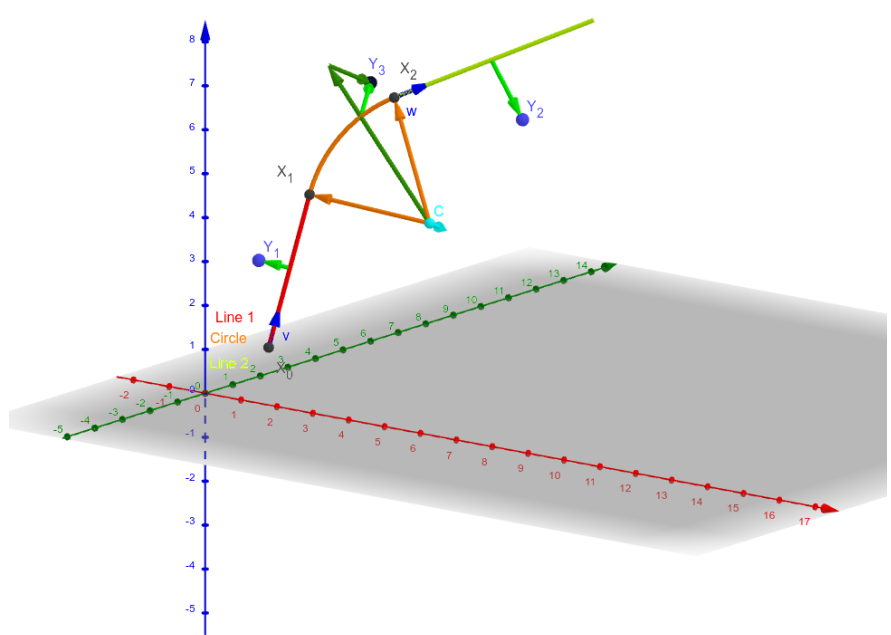


Figure 4.4: Circle and Lines Fit 3D geometry. Swap for better image.

Conclusion

741 Here or at the end of each section. Something about the future of this work?

Notes

743 General notes about the thesis:

- 744 • Check that all of the classes and other code are marked the same way in
745 the text. I used italics somewhere, could use different font for this instead.
- 746 • Check unbreakable space in front of articles. Remove excessive article usage
747 with proper nouns.
- 748 • Currently using margins for single-sided printing (bigger on the left side).
- 749 • Check that present tense is used
- 750 • American English quotation marks (") instead of British English (').
- 751 • Some of the overfull hbox warnings might change if duplex printing is used
752 (they generate black rectangles on the edge of the page), leaving them be
753 for now
- 754 • Check nobreakdash usage
- 755 • Check capitalized references (e.g., Figure, Section, Equation)
- 756 • Check $\backslash(...\backslash)$ math mode instead of $\$...$$. (actually unlike $\backslash[...\backslash]$ math mode,
757 there is apparently no real benefit to this clumsy syntax)
- 758 • Use siunitx package to ensure correct formatting.
- 759 • Check other stuff that's written in the MFF UK template.
- 760 • Check correct subscripts in equation (italics vs no italics)

761 Random notes:

- 763 • Terminology consistency – ionization/primary/secondary electrons
- 764 • Only electrons that start and end in the sector closer than 0.5 cm are used
765 for reconstruction (newest version).

Future

767 Things planned for the future:

- 768 • Testing the reconstruction algorithm by measuring real particles with a known
769 energy distribution.
- 770 • The **Fast Simulation with Ionization Electron Map** is planned for
771 the future. It will use the HEED program [25] to simulate the primary par-
772 ticle and the Ionization Electron Map (see Section 3.2) to simulate the drift
773 of secondary electrons. It should be significantly faster than the Microscopic

774 Simulation but offer comparable precision since it will rely on an already
775 simulated drift map. (Primary track simulated in HEED. Readout parameters
776 by interpolating the map. Diffusion from the map for randomization.)

- 777 • Account for GEM, delta electrons, ...
- 778 • Likelihood approach instead of least squares (if it improves the reconstruction
779 significantly), we should at least use a better method than taking
780 the center of the TPC bin.
- 781 • More detailed electric field simulation (if needed, GEM will have more com-
782 plex field)

783 Likelihood - inverse map

784 If we wanted to further improve this procedure, taking into account the whole
785 map \mathcal{M} , we could make an "inverse map" from \mathcal{R} to distributions on \mathcal{D} . We could
786 achieve this by taking the normalized probability density of an electron with initial
787 coordinates (x, y, z) having readout coordinates (x', y', t) . If we fix (x', y', t) , we
788 get an unnormalized probability density $f(x, y, z) = \mathcal{M}_{(x,y,z)}(x', y', t)$ (assuming
789 that all initial coordinates are a priori equally likely). This could potentially
790 improve the discrete reconstruction if we take the mean value of this probability
791 density across the pad and time bin

$$f_{\text{pad, bin}}(x, y, z) = \frac{1}{A_{\text{pad}} \Delta t_{\text{bin}}} \int_{\text{pad, bin}} \mathcal{M}_{(x,y,z)}(x', y', t) dx' dy' dt \quad (4.20)$$

792 and using it for a likelihood fit instead of using least squares. This still assumes
793 that all initial coordinates are equally likely which is clearly not the case for
794 a primary particle track. In the future, we could even use the fast track simulation
795 with the map (should be possible to make around 1000 tracks per minute per core
796 with current settings), create a big set of tracks with reasonable parameters and
797 use these to get an approximation of the probability distribution of the detector
798 response. Some approximations would be necessary when interpreting the data to
799 decrease the degrees of freedom of this distribution (we would have to pick a set of
800 parameters and assume that some of them are independent). This could give us
801 an idea about the best achievable resolution (how significantly will the detector
802 response differ for a given change in energy). If the difference is significant, we
803 could try to further improve the likelihood fit.

Bibliography

- [1] Garfield++. <https://garfieldpp.web.cern.ch/garfieldpp/>. Accessed: 2023-05-18.
- [2] Rene Brun and Fons Rademakers. Root — An Object Oriented Data Analysis Framework. *Nuclear Instruments and Methods in Physics Research Section A: Accelerators, Spectrometers, Detectors and Associated Equipment*, 389(1–2):81–86, Apr 1997. Proceedings AIHENP’96 Workshop, Lausanne, Sep. 1996, See also <https://root.cern/>, Paper published in the Linux Journal, Issue 51, July 1998.
- [3] About MetaCentrum. <https://metavo.metacentrum.cz/en/about/index.html>, 2023. Accessed: 2024-11-27.
- [4] M. E. Rose. Internal Pair Formation. *Phys. Rev.*, 76:678–681, Sep 1949.
- [5] R. Essig, J. A. Jaros, W. Wester, P. Hansson Adrian, S. Andreas, T. Averett, O. Baker, B. Batell, M. Battaglieri, J. Beacham, T. Beranek, J. D. Bjorken, F. Bossi, J. R. Boyce, G. D. Cates, A. Celentano, A. S. Chou, R. Cowan, F. Curciarello, H. Davoudiasl, P. deNiverville, R. De Vita, A. Denig, R. Dharmapalan, B. Dongwi, B. Döbrich, B. Echenard, D. Espriu, S. Fegan, P. Fisher, G. B. Franklin, A. Gasparian, Y. Gershtein, M. Graham, P. W. Graham, A. Haas, A. Hatzikoutelis, M. Holtrop, I. Irastorza, E. Izaguirre, J. Jaeckel, Y. Kahn, N. Kalantarians, M. Kohl, G. Krnjaic, V. Kubarovský, H-S. Lee, A. Lindner, A. Lobanov, W. J. Marciano, D. J. E. Marsh, T. Maruyama, D. McKeen, H. Merkel, K. Moffeit, P. Monaghan, G. Mueller, T. K. Nelson, G. R. Neil, M. Oriunno, Z. Pavlovic, S. K. Phillips, M. J. Pivovaroff, R. Poltis, M. Pospelov, S. Rajendran, J. Redondo, A. Ringwald, A. Ritz, J. Ruz, K. Saenboonruang, P. Schuster, M. Shinn, T. R. Slatyer, J. H. Steffen, S. Stepanyan, D. B. Tanner, J. Thaler, M. E. Tobar, N. Toro, A. Upadye, R. Van de Water, B. Vlahovic, J. K. Vogel, D. Walker, A. Weltman, B. Wojtsekhowski, S. Zhang, and K. Zioutas. Dark Sectors and New, Light, Weakly-Coupled Particles, 2013.
- [6] F.W.N. de Boer, O. Fröhlich, K.E. Stiebing, K. Bethge, H. Bokemeyer, A. Balandia, A. Buda, R. van Dantzig, Th.W. Elze, H. Folger, J. van Klinken, K.A. Müller, K. Stelzer, P. Thee, and M. Waldschmidt. A deviation in internal pair conversion. *Physics Letters B*, 388(2):235–240, 1996.
- [7] F W N de Boer, R van Dantzig, J van Klinken, K Bethge, H Bokemeyer, A Buda, K A Müller, and K E Stiebing. Excess in nuclear pairs near 9 MeV/ invariant mass. *Journal of Physics G: Nuclear and Particle Physics*, 23(11):L85, nov 1997.
- [8] F W N de Boer, K Bethge, H Bokemeyer, R van Dantzig, J van Klinken, V Mironov, K A Müller, and K E Stiebing. Further search for a neutral boson with a mass around 9 MeV/c². *Journal of Physics G: Nuclear and Particle Physics*, 27(4):L29, apr 2001.

- 845 [9] Attila Vitéz, A. Krasznahorkay, J. Gulyas, Margit Csatlos, Lorant Csige,
 846 Zoltan Gacsi, Barna Nyakó, F. Boer, T. Ketel, and J. Klinken. Anomalous
 847 Internal Pair Creation in ${}^8\text{Be}$ as a Signature of the Decay of a New Particle.
 848 *Acta Physica Polonica B - ACTA PHYS POL B*, 39:483, 02 2008.
- 849 [10] A. Krasznahorkay, J. Gulyas, Margit Csatlos, Attila Vitéz, T. Tornyi,
 850 L. Stuhl, Lorant Csige, Zoltan Gacsi, A. J. Krasznahorkay, M. Hunyadi,
 851 and T.J. Ketel. Searching for a light neutral axial-vector boson in isoscalar
 852 nuclear transitions. *Frascati Physics Series*, 56:86, 10 2012.
- 853 [11] A. J. Krasznahorkay, M. Csatlós, L. Csige, Z. Gácsi, J. Gulyás, M. Hunyadi,
 854 I. Kuti, B. M. Nyakó, L. Stuhl, J. Timár, T. G. Tornyi, Zs. Vajta, T. J. Ketel,
 855 and A. Krasznahorkay. Observation of Anomalous Internal Pair Creation
 856 in ${}^8\text{Be}$: A Possible Indication of a Light, Neutral Boson. *Physical Review
 857 Letters*, 116(4), January 2016.
- 858 [12] D.R. Tilley, J.H. Kelley, J.L. Godwin, D.J. Millener, J.E. Purcell, C.G. Sheu,
 859 and H.R. Weller. Energy levels of light nuclei $A=8,9,10$. *Nuclear Physics A*,
 860 745(3):155–362, 2004.
- 861 [13] N. J. Sas, A. J. Krasznahorkay, M. Csatlós, J. Gulyás, B. Kertész, A. Krasznahorkay,
 862 J. Molnár, I. Rajta, J. Timár, I. Vajda, and M. N. Harakeh. Observation
 863 of the X17 anomaly in the ${}^7\text{Li}(p,e^+e^-){}^8\text{Be}$ direct proton-capture
 864 reaction, 2022.
- 865 [14] A. J. Krasznahorkay, M. Csatlós, L. Csige, J. Gulyás, A. Krasznahorkay,
 866 B. M. Nyakó, I. Rajta, J. Timár, I. Vajda, and N. J. Sas. New anomaly
 867 observed in ${}^4\text{He}$ supports the existence of the hypothetical X17 particle.
 868 *Physical Review C*, 104(4), October 2021.
- 869 [15] D.R. Tilley, H.R. Weller, and G.M. Hale. Energy levels of light nuclei $A =$
 870 4. *Nuclear Physics A*, 541(1):1–104, 1992.
- 871 [16] A. J. Krasznahorkay, A. Krasznahorkay, M. Begala, M. Csatlós, L. Csige,
 872 J. Gulyás, A. Krakó, J. Timár, I. Rajta, I. Vajda, and N. J. Sas. New
 873 anomaly observed in ${}^{12}\text{C}$ supports the existence and the vector character of
 874 the hypothetical X17 boson. *Phys. Rev. C*, 106:L061601, Dec 2022.
- 875 [17] F. Ajzenberg-Selove. Energy levels of light nuclei $A = 11,12$. *Nuclear Physics
 876 A*, 506(1):1–158, 1990.
- 877 [18] Péter Kálmán and Tamás Keszthelyi. Anomalous internal pair creation. *The
 878 European Physical Journal A*, 56, 08 2020.
- 879 [19] A. Aleksejevs, S. Barkanova, Yu. G. Kolomensky, and B. Sheff. A Standard
 880 Model Explanation for the "ATOMKI Anomaly", 2021.
- 881 [20] Jonathan L. Feng, Bartosz Fornal, Iftah Galon, Susan Gardner, Jordan
 882 Smolinsky, Tim M. P. Tait, and Philip Tanedo. Protophobic Fifth-Force
 883 Interpretation of the Observed Anomaly in ${}^8\text{Be}$ Nuclear Transitions. *Phys.
 884 Rev. Lett.*, 117:071803, Aug 2016.

- 885 [21] Tran The Anh, Tran Dinh Trong, Attila J. Krasznahorkay, Attila Krasznahorkay,
886 József Molnár, Zoltán Pintye, Nguyen Ai Viet, Nguyen The Nghia,
887 Do Thi Khanh Linh, Bui Thi Hoa, Le Xuan Chung, and Nguyen Tuan Anh.
888 Checking the ${}^8\text{Be}$ Anomaly with a Two-Arm Electron Positron Pair Spec-
889 trometer. *Universe*, 10(4):168, April 2024.
- 890 [22] Kh. U. Abraamyan, Ch. Austin, M. I. Baznat, K. K. Gudima, M. A. Kozhin,
891 S. G. Reznikov, and A. S. Sorin. Observation of structures at ~ 17 and ~ 38
892 MeV/c 2 in the $\gamma\gamma$ invariant mass spectra in pC, dC, and dCu collisions at
893 p_{lab} of a few GeV/c per nucleon, 2023.
- 894 [23] The MEG II collaboration, K. Afanaciev, A. M. Baldini, S. Ban, H. Ben-
895 mansour, G. Boca, P. W. Cattaneo, G. Cavoto, F. Cei, M. Chiappini,
896 A. Corvaglia, G. Dal Maso, A. De Bari, M. De Gerone, L. Ferrari
897 Barusso, M. Francesconi, L. Galli, G. Gallucci, F. Gatti, L. Gerritzen,
898 F. Grancagnolo, E. G. Grandoni, M. Grassi, D. N. Grigoriev, M. Hilde-
899 brandt, F. Ignatov, F. Ikeda, T. Iwamoto, S. Karpov, P. R. Kettle, N. Kho-
900 mutov, A. Kolesnikov, N. Kravchuk, V. Krylov, N. Kuchinskiy, F. Leonetti,
901 W. Li, V. Malyshev, A. Matsushita, M. Meucci, S. Mihara, W. Mol-
902 zon, T. Mori, D. Nicolò, H. Nishiguchi, A. Ochi, W. Ootani, A. Oya,
903 D. Palo, M. Panareo, A. Papa, V. Pettinacci, A. Popov, F. Renga, S. Ritt,
904 M. Rossella, A. Rozhdestvensky, S. Scarpellini, P. Schwendimann, G. Sig-
905 norelli, M. Takahashi, Y. Uchiyama, A. Venturini, B. Vitali, C. Voena,
906 K. Yamamoto, R. Yokota, and T. Yonemoto. Search for the X17 particle
907 in ${}^7\text{Li}(p, e^+e^-){}^8\text{Be}$ processes with the MEG II detector, 2024.
- 908 [24] Misbah Uddin Ahmed. Simulation of the electron and ion movement through
909 a 4-GEM stack, 2021. Institut für Kernphysik.
- 910 [25] I.B. Smirnov. Modeling of ionization produced by fast charged particles in
911 gases. *Nuclear Instruments and Methods in Physics Research Section A: Ac-
912 celerators, Spectrometers, Detectors and Associated Equipment*, 554(1):474–
913 493, 2005.
- 914 **Acknowledgments:** Computational resources were provided by the e-INFRA
915 CZ project (ID:90254), supported by the Ministry of Education, Youth and Sports
916 of the Czech Republic.

917 List of Figures

| | | |
|--------------|---|----|
| 918 0.1 | The ATOMKI anomalous IPC measured for different nuclei. | 5 |
| 919 0.2 | Results from the Hanoi spectrometer – angular e^+e^- pair correlations measured in the ${}^7\text{Li}(p, e^+e^-){}^8\text{Be}$ reaction at $E_p = 1225$ keV [21]. | 6 |
| 920 0.3 | Results from the MEG II experiments – angular correlation of e^+e^- pairs with $E_{\text{sum}} \in [16, 20]$ MeV measured in the ${}^7\text{Li}(p, e^+e^-){}^8\text{Be}$ reaction with proton beam energies 500 and 1080 keV. The 500 keV dataset is fitted with Monte Carlo of both the IPC deexcitation and the EPC produced by gammas [23]. | 7 |
| 921 0.4 | Schematics of the detector at the Van der Graaff facility at IEAP CTU. | 7 |
| 922 1.1 | Garfield simulation of an avalanche in a GEM hole [24]. | 11 |
| 923 1.2 | Schematics of the first sector OFTPC with detector space coordinates. | 13 |
| 924 1.3 | Pad layout of the OFTPC and its parameters. | 14 |
| 925 1.4 | Magnetic field simulation results. OFTPC volume is marked with black lines. | 15 |
| 926 1.5 | Visualization of trilinear interpolation as a composition of linear interpolations. <i>Image drawn in GeoGebra and inspired by a similar image on Wikipedia (which looks a bit worse) – is credit necessary?</i> | 16 |
| 927 2.1 | Example of a simulated electron track in 70 % argon and 30 % CO ₂ atmosphere (on the left). <i>Swap for better images, better zoom. Explain drift lines, primary particle.</i> | 18 |
| 928 2.2 | Comparison of diffusion in a simulated electron track in 70 % argon, 30 % CO ₂ atmosphere and in 90 % argon, 10 % CO ₂ atmosphere (on the right). <i>Swap for better image, better zoom. Or put the same pictures for both comparisons in one subfigure, etc. Describe better.</i> | 18 |
| 929 3.1 | Dependence of the drift time on the z coordinate in 90 % argon and 10 % CO ₂ atmosphere, fitted with a linear function. The fitted function gives us the average drift velocity in the gas and can be used for rough reconstruction in our TPC. <i>Swap for better image with axis labels, etc. Maybe write the fitted equation.</i> | 20 |
| 930 3.2 | First attempt at a track reconstruction using only the drift velocity. This approach works well in a standard TPC (<i>ideally cite some source?</i>). 90 % argon and 10 % CO ₂ atmosphere. <i>Swap for better image, correct coordinates.</i> | 21 |
| 931 3.3 | First attempt at a track reconstruction using only the drift velocity, residues. <i>Swap for better image, correct coordinates. What's causing the shift? Explain details.</i> | 21 |
| 932 3.4 | Example of map generation. <i>Swap for better image, correct coordinates.</i> | 23 |
| 933 3.5 | Example reconstruction with the map. <i>Swap for better image, correct coordinates.</i> | 24 |

| | | | |
|-----|-----|---|----|
| 960 | 3.6 | Selection of the points for interpolation. Create better images; use the explanation interpolation vs. extrapolation strange property. Solution 2 probably does not make much sense. | 26 |
| 963 | 4.1 | Example of a fitted reconstructed track. Swap for better image. . | 28 |
| 964 | 4.2 | First attempt at a track reconstruction using only the drift velocity. Spline energy reconstruction attempt. Swap for better image(s) – subfigure environment, correct coordinates. | 30 |
| 967 | 4.3 | First attempt at a track reconstruction using only the drift velocity. Circle and Lines Fit in 2D. Swap for better image, correct coordinates. | 32 |
| 969 | 4.4 | Circle and Lines Fit 3D geometry. Swap for better image. | 33 |
| 970 | | | |

₉₇₁ **List of Tables**

⁹⁷² List of Abbreviations

- ⁹⁷³ **GEM** Gas Electron Multiplier
- ⁹⁷⁴ **HEED** High Energy Electro-Dynamics
- ⁹⁷⁵ **IEAP CTU** Institute of Experimental and Applied Physics, Czech Technical
⁹⁷⁶ University in Prague
- ⁹⁷⁷ **IPC** Internal Pair Creation
- ⁹⁷⁸ **EPC** External Pair Creation
- ⁹⁷⁹ **Micromegas** MICRO-MEsh GAseous Structure
- ⁹⁸⁰ **MWPC** Multi-Wire Proportional Chamber
- ⁹⁸¹ **OFTPC** Orthogonal Fields TPC
- ⁹⁸² **TPC** Time Projection Chamber
- ⁹⁸³ **ToA** time-of-arrival
- ⁹⁸⁴ **ToT** time-over-threshold
- ⁹⁸⁵ **Tpx3** Timepix 3